Hamburg University of Technology

Institute for Ship Structural Design and Analysis
Am Schwarzenberg-Campus 4 in D-21073 Hamburg

Project Thesis

Compression Tests of Laboratory-made Freshwater Ice

Robin Härer

Matriculation - No.: 21155748
robin.haerer@tu-harburg.de

Examiner: Prof. DSc. (Tech.) Sören Ehlers (TUHH)
Supervisor: M.Sc. Hauke Herrnring (TUHH)

Handover Date: March 13, 2019

Statement of Authorship

I certify that this project thesis has been composed by myself, and describes my own work, unless otherwise acknowledged in the text. All references and verbatim extracts have been quoted, and all sources of information have been specifically acknowledged. It has not been accepted in any previous application for a degree.

Location, Date

Signature

Acknowledgment

This project thesis entitled "Compression Tests of Laboratory-made Freshwater Ice" was made at the institute for Ship Structural Design and Analysis at the Hamburg University of Technology.

During the drafting, I was supervised by Prof. DSc. (Tech.) Sören Ehlers and M.Sc. Hauke Herrnring. At this point, I would like to give thanks for their pleasant and constantly professional support.

Additionally, I would like to give thanks to M.Sc. Jan M. Kubiczek and Andrzej Iwaszko who also led to the success of this thesis by supporting me at all times.

Also I want to thank all the employees of the institutes testing hall who stood me aside with help and advice for questions and practical challenges.

Furthermore, I would like to give thanks to Lucia Härer for proofreading this project thesis. She pointed out weaknesses and was able to suggest improvements while being a non-professional.

Last of all, I want to thank my family and friends for supporting me throughout this whole process.

Hamburg, March 2019

Robin Härer

Abstract

The knowledge of the characteristics of ice is important for the construction of vessels and offshore structures, challenging ice in polar regions. In ice-structure-interactions, ice often fails under compression, but the mechanisms behind along with the properties caused by the formation process are not understood completely yet.
To expand this knowledge, a number of uniaxial compression tests of three different fabrication methods of laboratory made freshwater ice have been conducted for this thesis to examine the influence of the inner structure on compressive strength values. After determining the most suitable fabrication procedure, the speed dependency of the compression strength and the failure modes of ice are analyzed and discussed by using the results of simple compression tests at different axial strain rates.
For these tests, a newly installed experimental set-up in a separate cold room is used for the first time. The pressure measuring system TekScan coupled with a high-speed camera is called into action to determine the strength values and the failure modes.

For the three investigated production methods significant structural and mechanical differences have been recorded. As observed in earlier research, some test series have a high degree of scattering strength values depending on the experimental speed. As a result none of the production methods shows promising results in terms of reproducibility. Nevertheless it has been possible to observe the speed dependence of the compression strength and the different failure modes based on one selected production method.

Contents

List of Figures

List of Tables

List of Symbols and Acronyms

Acronyms

CCI	Commercial Crushed Ice
DF	Deep Freezer
DW	Distilled Water
COV	Coefficient Of Variation
PVC	Polyvinyl Chloride
SMCI	Self-Made Crushed Ice

Greek Symbols

ϵ	Strain
$\dot{\epsilon}$	Strain rate
ϵ_e	Elastic strain rate
μ	Friction coefficient
σ	Stress
σ_c	Compressive strength

Latin Symbols

a	Mean grain area
A_0	Area of a defined circle
B	Creep constant
D	Diameter
d	Equivalent diameter
E	E-modulus
F	Force
F_{cyl}	Cylinder force
K_I	Stress intensity factor
K_{IC}	Critical stress intensity factor
m	Displacement
N	Total number of grains
N_1	Number of grains within the defined circle area A_0
N_2	Number of grains on the perimeter of the defined circle
R	Confinement ratio
t	Time

1 Introduction

The activities in arctic and subarctic regions have significantly increased in the recent years like seen in Figure 1. The expansion of the offshore oil and gas industry plays an important role due to limitations of natural resources in other parts of the planet. Additional increasing world trade and global warming facilitate the utilization of new shipping routes guiding into ice covered regions. According to Humpert and Raspotnik (2012) [15] the decrease of the ice coverage will open main shipping routes for more than 120 days, even in the middle of this century with a potential for savings of up to 40 percent. In addition, the touristic interest for cruises into the remaining polar regions ascends [33].

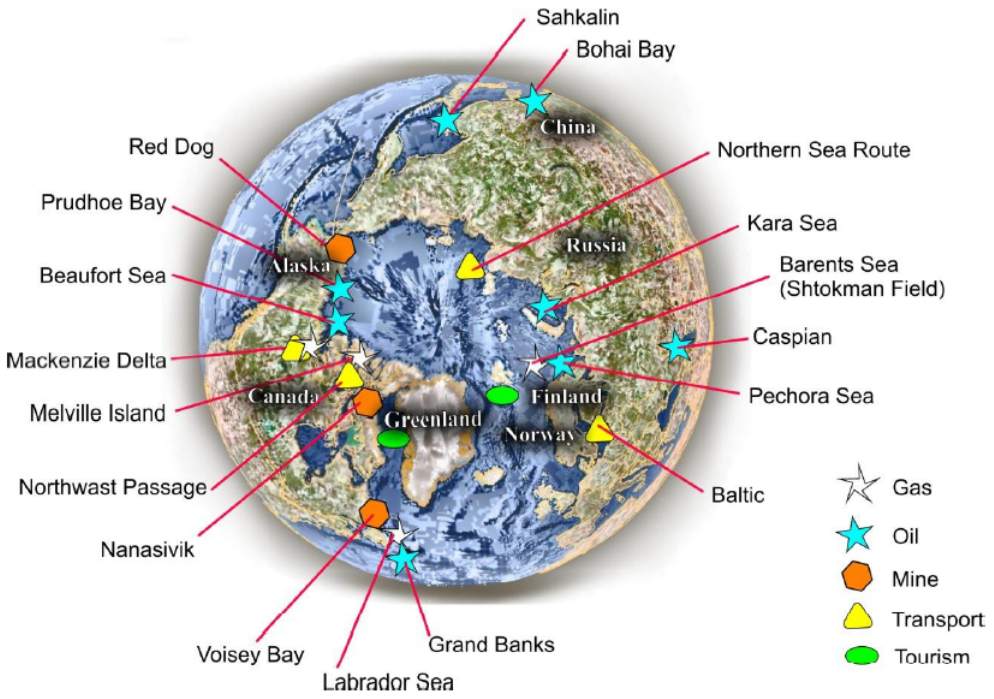

Figure 1: Current ice engineering activities [3]

Secure and economic undertakings in such areas underscore the need for improved methods for the design of engineered vessels and offshore structures operating in the prevailing conditions. Therefore a deeper knowledge about the structural properties and the mechanical behavior of ice is needed.

When ice collides with a vessel or an offshore structure, it often fails under compressive loads so that the compressive strength is a fundamental quantity and often used for empirical design formulas. In this context, either data from local measurements or from small-scale model tests are of particular importance to predict the possible ice loads in real ice-structure-interactions and thus to design ice-going structures. The small-scale model tests have the advantage that they can be performed in a controlled environment

with known material properties. And although ice is a very common phenomenon, its exact formation and behavior under load is not investigated completely yet. This is the origin of the idea for this thesis which is part of a research program of the institute for Ship Structural Design and Analysis at the Hamburg University of Technology. By means of a newly installed experimental assembly, ice compression tests of three different production methods of laboratory-made freshwater ice are carried out in this scope. The aim is to achieve reproducible specimen and to gain insights into the internal structure of the specimen as well as to evaluate their influence on the compressive strength. Since the compression strength depends on the strain rate, a uniform experimental speed is selected to compare the three methods. Furthermore, from the series with the most appropriate results, the speed dependence of the compressive strength and failure modes is shown. The specimen are generated in a cold room under laboratory conditions. Two of the three production methods make use of different types of crushed ice to achieve a homogeneous and granular grain structure that simplifies the study of ice deformation behavior. The third method of columnar grown ice serves as a reference and comparison on previous researches. To determine the failure modes, the pressure measuring system TekScan coupled with a high-speed camera is used so that a possible correlation between the failure mode and the achieved compression strength can be reviewed. The evaluation of the tests includes strength characteristics and failure modes within a statistical consideration of the results.

At the beginning of this work, an overview of the properties of water and ice can be found. Chapter 3 gives an introduction of the mechanical behavior of ice under compression and the mechanisms behind. The following chapter 4 shows the experimental part and describes the preparation of the specimen as well as the test setup and configurations. In chapter 5, the observations during the tests as well as the recorded data are given. The evaluation of the conducted tests is presented in chapter 6. A summary of the results, along with suggestions for further researches, is given at the end of the thesis.

2 Structure of Ice

By the renewed interest in polar regions, the construction of ships operating out there has to move to a more informed approach. For a better understanding of the failure processes in ice-structure interactions, the structural composition of ice must be understood first. In doing so we initially have a look at possible manifestations and then go deeper into the crystal structure and its lattice defects which play a major role in regard of failure.

Depending on the freezing circumstances, there are different super-coordinate structures and molecular arrangements of water which will be shown in the phase diagram in Figure 2. As known so far, ice possesses twelve possible crystalline forms and two amorphous states depending on the temperature and the ambient pressure [29].

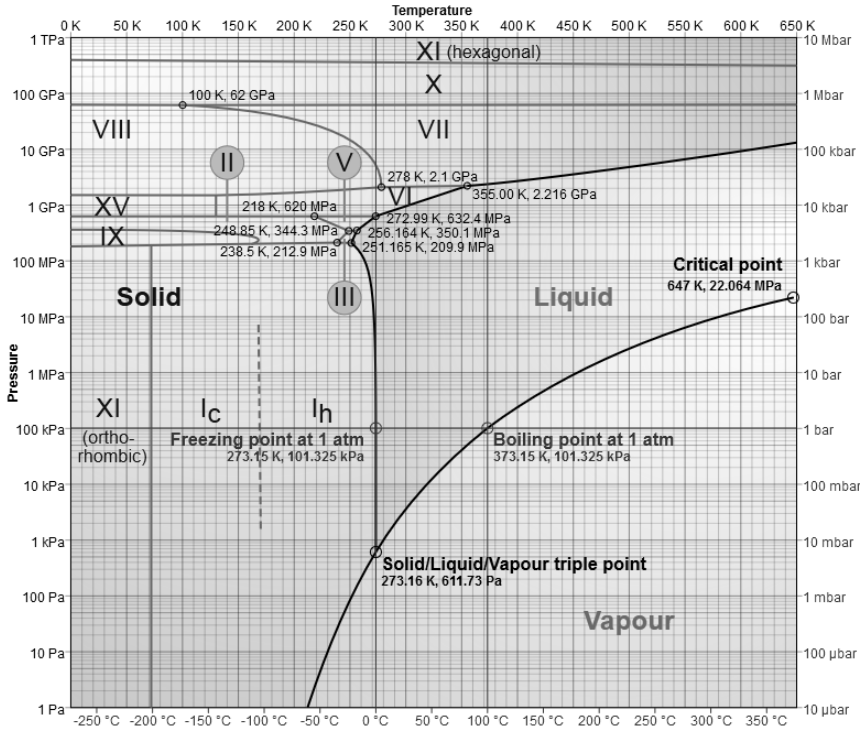

Figure 2: Water phase diagram [1]

Referring to Figure 2 it can be seen that only the ice structures with the designation I can exist at ordinary pressure. Therefore, three closely related variants of crystallographic structures are known [23]:

- The hexagonal structure (I_h)
- The cubic structure (I_c)
- The amorphous structure

Only the hexagonal structure I_h, termed ordinary ice can be found in nature because it is stable down to normal low temperatures and an ambient pressure [30]. All other crystallographic structures have only been observed in the laboratory. Researches and further discussions are found in Hobbes (2010) [12].
Within the scope of this thesis we address the structure of ordinary ice I_h in the following subsections. In relation to the failure mechanism, the important elements include the crystal structure as well as the defect structure with its point-, line-, planar- and volumetric- features. Dislocations play an essential role in creep and also in the formation of micro-cracks as well as in the evolution of the micro-structure [35].

2.1 Crystal Structure

In its common terrestrial form, ordinary ice shows up in a hexagonal crystal structure as presented in Figure 3. Thereby each water molecule is surrounded by four neighboring molecules which are located near the vertices of a regular tetrahedron centered about the molecule of interest [29]. The oxygen atom of each water molecule shares a pair of electrons with each of the two hydrogen atoms which enter into strong covalent bonds. Due to the dipole, water molecules occupy intermolecular attractive forces and can develop hydrogen bridge bonds to contiguous water molecules. Thereby a hydrogen atom with a positive partial charge orientates to a negatively charged oxygen atom of a neighboring water molecule. These inter-linkages of hydrogen bridge bonds are not as strong as covalent bonds but are account for a lot of specific properties of water [23].

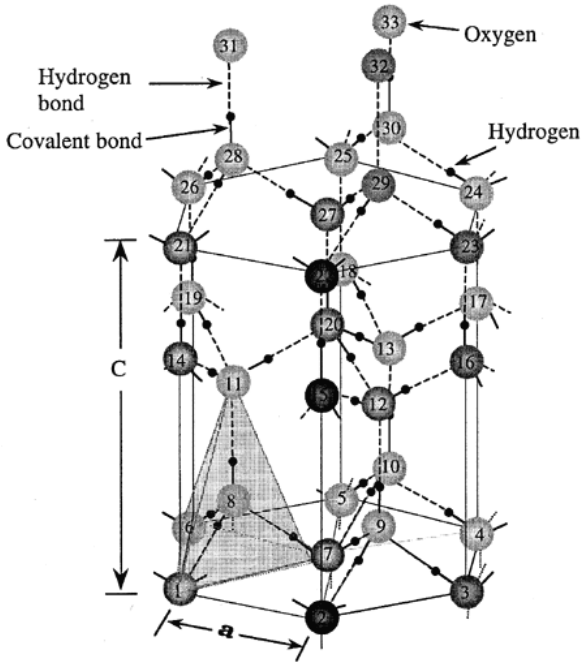

Figure 3: Molecular arrangement of the hexagonal ice structure [29]

Based on Figure 3, a number of important features of the molecular structure of ice can be shown. The lattice parameters near the melting point are a = 0.4523 nm and c =

0.7367 nm. The ratio of these items of about 1.628 is very close to the ideal c/a ratio of 1.633 and is independent of temperature. Compared to liquid water, the unit cell which represents the fundamental building block of the crystallographic structure of I_h ice is relatively open effecting a lower density of ordinary ice [29].

The oxygen atoms form rings that are projected into the so-called basal planes that have the closest packing in the structure of I_h ice. The hydrogen atoms whose positions in the ice molecule are not as well discovered as the positions of the oxygen atoms, are arranged randomly according to the Bernal-Fowler rules (1933). These rules state that each oxygen atom has two covalently bonded hydrogen atoms, and additionally that the oxygen atom in each water molecule forms two hydrogen bonds with other oxygens, so that there is exactly one hydrogen atom on each O-O bond [23]. Due to the extraordinarily slow reorientation of the water molecule at low temperatures, the random arrangement persists and ice can appear in various configurations with different distributions of the hydrogen atoms under natural conditions [29].

2.2 Defect Structure

The structure of ice is characterized by various defects that occur in the atomic lattice. Based on their deposit, the ice structure gets its various mechanical behavior.

2.2.1 Point Defects

The point defects are important for the description of the inelastic behavior, particularly creep. According to Schulson and Duval (2009) [30] they can be divided in:

- Vacancies
- Interstitials
- Solutes
- Ionic and Bjerrum defects

Schulson (1999) [29] claims that the hydrogen- and oxygen atom have the same diffusion coefficient in ordinary ice which means that the coherent H_2O molecule moves as a unit. Due to the fact that the activation energy of this process is nearly the same as the added energy of vacancy formation and migration, Schulson (1999) [29] assumes that vacancies are the main point defect. However, recent studies of another source [37] about the annealing of dislocations indicates that interstitials are the deciding point defect. Ionic and Bjerrum defects occur owing to nonobservances of the Bernal-Fowler rules. If one proton (H^+) moves along a O-O bond and passes from one water molecule over to another, the first rule is violated. As a consequence the proton near the oxygen atom creates an OH^- ion and three positive protons create an H_3O^+ ion. The second rule gets violated if the proton moves around the oxygen atom. This leads to a so called L-type Bjerrum defect since there is no hydrogen atom on the O-O bond. Two protons create a D-type Bjerrum defect. In this case the "L" stands for "empty" and the "D" for "doublet".

2.2.2 Line Defects

Of greater significance concerning the behavior of ice under load especially plastic behavior, are dislocations which are line defects located in the lattice of a crystal that allow an easier shift to the atomic planes [23]. Dislocations can be divided into three types like seen in Figure 4:

- Edge dislocations
- Screw Dislocation
- Mixed Dislocation

The two basic types are described by the Burger's vector, that presents the direction of propagation and the amount of displacement. In an edge dislocation, there is an additional atomic plane in one part of the crystal. This plane is oriented perpendicular to the sliding direction and moves on a horizontal plane (sliding plane) through the crystal lattice. Therefore the burger's vector is perpendicular to the edge dislocation. In turn the screw dislocation is parallel to this vector and can also skip to other atomic planes. This property is called cross-slip [30]. This type of dislocation occurs parallel to the sliding direction, whereas the sliding plane is oriented perpendicular to the sliding direction. In natural crystals, however, mostly mixed dislocations occur that means mixed forms which containing components of both types.

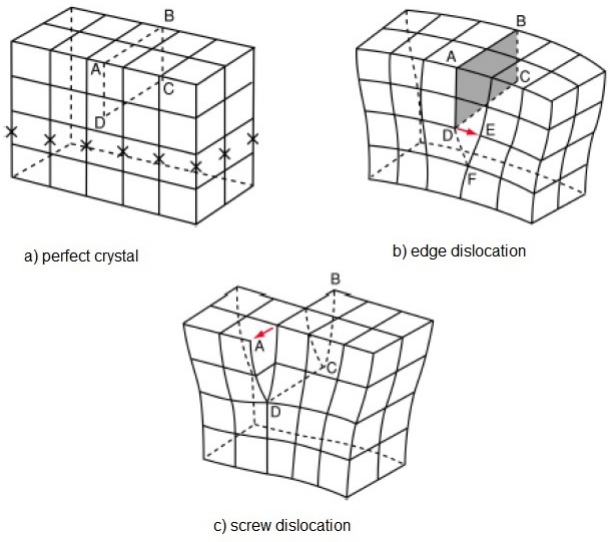

Figure 4: Types of dislocations in hexagonal ice structure [13]

2.2.3 Planar Defects

A planar defect is a two-dimensional lattice defect in the crystal structure. They are formed most likely in the densest packed crystal planes, since the interaction between the atoms is the strongest there. In addition to free surfaces, the planar defect leads

to the formation of grain boundaries and thus prevents the formation of monocrystals [30]. Planar defects occur, for example, as a result of twinning (not yet observed in the ice crystal) or when a partial dislocation passes through the crystal. Near the melting point, the grain boundaries have liquid water in sub-millimeter-sized veins (in sea ice additional brine pockets) and are places of slip and crack formation and thus crucial microstructural features [29].

2.2.4 Volumetric Defects

After Michel (1978) [23] the most common volumetric defect is pores. Through the solidification process of ice, pores form as the result of rejecting oxygen and nitrogen from water as well as from the ice lattice. In the case of fresh-water ice they only conclude air. When we talk about salt-water ice, they can also consist of brine [30]. Hard particles also fall under the description of volumetric defects which can be found as atmospheric particulates that can become entrapped via either dry deposition on the snow or during the nucleation of ice crystals [30]. While pores tend to lower the resistance to creep deformation, hard particles can do both increase and decrease the creep resistance, depending on their size and density as well as on the temperature of the ice. Pores also lower the resistance to crack propagation [35].

2.3 Microstructure

In this subsection we take a look at the variety of the microstructure of ordinary ice. Natural grown ice formations often exhibit a rich and varied microstructure that depends on the thermal-mechanical history and entrapped inclusions [23]. With the exception of snow-flakes and some icicles, all natural ice bodies are polycrystals [30]. Depending on the conditions during the formation process different internal structures can arise. The respective grain size typically can vary from millimeters to several centimeters while the grain shape diversifies from equiaxed to elongated [32]. For instance glaciers and polar ice sheets are generally composed of equiaxed and randomly oriented grains that form through the sintering of snow under heat and pressure. The microstructure also effects different mechanical behaviors. In the latter case, the material behaves anisotropically [30] like treated later. In comparison, the arctic ice cover consists primarily of columnar-shaped grains which is a result of unidirectional solidification of salt water. Sea ice is also characterized by an intragranular porous substructure that consists of submillimeter diameter air bubbles and brine pockets that get entrapped during solidification [3]. To describe the orientation of the grains the c-axis is used, oriented perpendicular to the basal plane. For example the ice cover possesses a growth texture in which the crystallographic c-axes are more or less confined to the horizontal plane. That leads to geometric selection where favorable oriented grains grow along the crystallographic a-axes aligned parallel to the basal planes. Depending on the formation and the orientation of the c-axes, different ice types can be classified. A detailed description can be found in Michel (1978) [23].

After a brief insight into the internal structure of ice and its possible origins, the next step is to consider the behavior of this structure under mechanical loads. Due to the fact that ice often fails under compression in ice-structure interactions, the following chapters mainly focus on the behavior and the underlying mechanisms of ice under compression.

3 The Mechanical Behavior of Ice under Compression

To examine the mechanical behavior, we first observe a simplified monocrystal. In doing so a clear strength anisotropy can be recognized. When loading a single ice crystal, the resulting deformation is highly dependent on the direction of the introduced force relative to the direction of the ice crystals c-axis [18]. With a large angle to the c-axis, even a low shear stress is sufficient to cause deformation. This relates to the relatively weak bonds between the basal planes, which can barely resist a load. This type of deformation is called "easy glide" or gliding of the basal planes [30]. On the other hand, the crystal can hardly be deformed in the direction parallel to the c-axis which is called "hard glide" like demonstrated in Figure 5.

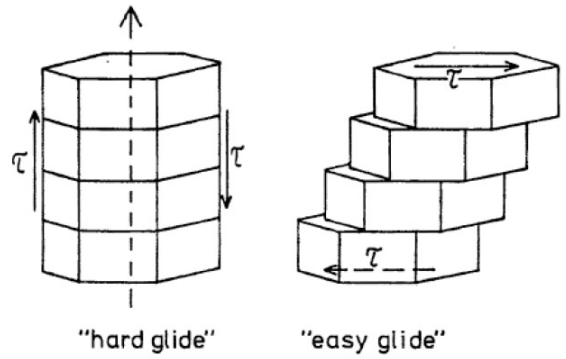

Figure 5: Comparison of hard and easy glide of a monocrystal [30]

The Young's modulus of single crystals varies from 12 GPa parallel to the c-axis to 10 GPa along directions within the basal plane [29].
Natural ice is polycrystalline and consists of several ice crystals as the name indicates. At the beginning of the deformation of polycrystals the elastic behavior is characterized by moderate anisotropy, since the c-axes still have no preferred orientation for basal sliding [16]. At higher loads, the flow properties of ice are mainly determined by intracrystalline sliding of dislocations so that the inelastic behavior of polycrystals is markedly anisotropic [4]. For randomly oriented polycrystals, typical values of Young's modulus and Poisson's ratio are 9.33 MPa and 0.33 at –5°C [29]

According to Schulson (1999) [29] the critical shear stress for non-basal slip is at least 60 times greater than that for basal slip. Due to this fact there is a problem for polycrystals. Schulson assumes that four independent deformation modes are required for broadly crack-free flow. But as basal slip allows only two independent deformation modes the

plastic anisotropy leads to the buildup of internal stresses under the further assumption that twinning does not occur. These stresses arise owing to grains favorably oriented for slip that shed load to those less well oriented so that plastic flow will initiate cracks if there is no time for the internal stresses to relax. If these cracks are taken, the ice will behave macroscopically ductile. On the other side if not, then the material will exhibit brittle behavior [29].
How the macroscopically behaviors are represented can be easily visualized by means of a graphical display of the stress-strain curve.

3.1 Stress-Strain-Curve

In the case of uniaxial compression, Figure 6 shows the schematic stress-strain curves for different strain rates. After Schulson (1999) [29] cracks do not form at very low rates (I) which results in ductile material behavior, indicated by a horizontal arrow. As a consequence of high rates of deformation, cracks initiate and the specimen gets brittle represented by curve III and a vertical oriented arrow. The transition between ductile and brittle material behavior occurs at intermediate strain rates like shown in curve II. The development of cracks requires a tensile stress which straight opens the cracks. Under compression this kind of tensile stress results of local crack sliding. Schulson (1999) [29] suspects that the peak in the stress-strain curve (II) is referable to crack-induced localized flow.

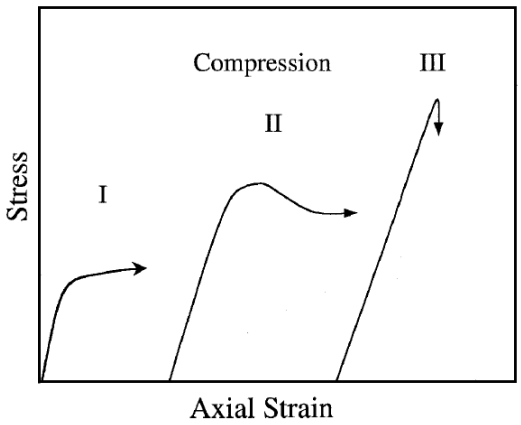

Figure 6: Schematic stress strain curves under compression [29]

Some observed experimental values of the compressive strength and the related strain rates are shown in Figure 7 as a compilation of different researchers. The values accrue from tests with equiaxed and randomly oriented fresh water ice of about 1 mm grain size at a temperature of about -10 °C. The annotations I, II, III accord to the stress-strain curves from the figure above. For ductile failure the term of strength is defined as the highest stress recorded during the test. In the case of brittle behavior, the failure stress serves as definition. The figure also shows the boundaries of the strain rates indicating a change of behavior for this type of ice. Brittle failure under compression is linked to small failure strains ($\epsilon \leq 0.5\%$) and higher strain rates ($\dot{\epsilon} \geq 10^{-3}$). For ductile behavior,

strains can be distinctly larger. Under very low strain rates, (here $\dot{\epsilon} \leq 10^{-5}$), ice can even sustain strains of more than one [30].

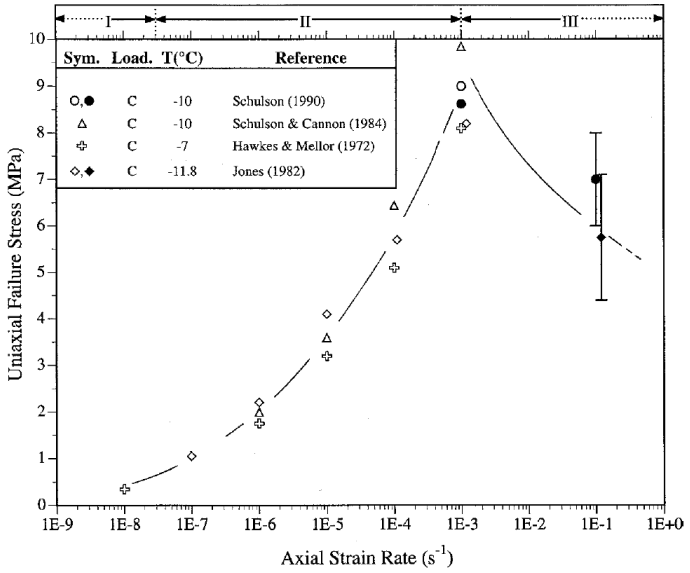

Figure 7: Compressive failure stress vs axial strain rate [29]

The exact mechanisms behind the individual behaviors of ice under compressive load, are shown in the next section.

3.2 The Mechanism of Ductile Failure under Compression

In order to explain the mechanisms of low-rate deformations, researches on natural ice formations like glaciers and ice sheets are prevalent. Although such low strain rates are less significant for ice interaction scenarios and not all mechanisms have been clarified yet, a brief overview is given here.
By the means of creep tests, the mechanical behavior of homogeneous granular ice like in glaciers is studied. Therefore the applied load is maintained at a constant value depending on the finite strain. Some researchers found out that there is a clear evidence that intracrystalline dislocation glide is the main deformation process in the case of polycrystalline glacier ice [3]. Like seen before the glide of dislocations on the basal plane and the cross-slip of basal dislocations are the subject of the behavior of single crystals. After Schulson (2009) [30] the climb of basal dislocations can also be applied to the deformation of polycrystalline ice. Strain can also be obtained by transporting matter in the way of diffusion or shear along grain boundaries. This so-called grain boundary sliding makes voids that can be accommodated when water molecules diffuse from compressed parts of the boundary to those that are in tension. That means the other way round, that diffusion creep creates the driving force for grain boundary sliding [30].

As a result of a creep test with constant loading of a homogeneous granular ice sample, Figure 8 is given. It represents a typical creep curve and states the strain over time.

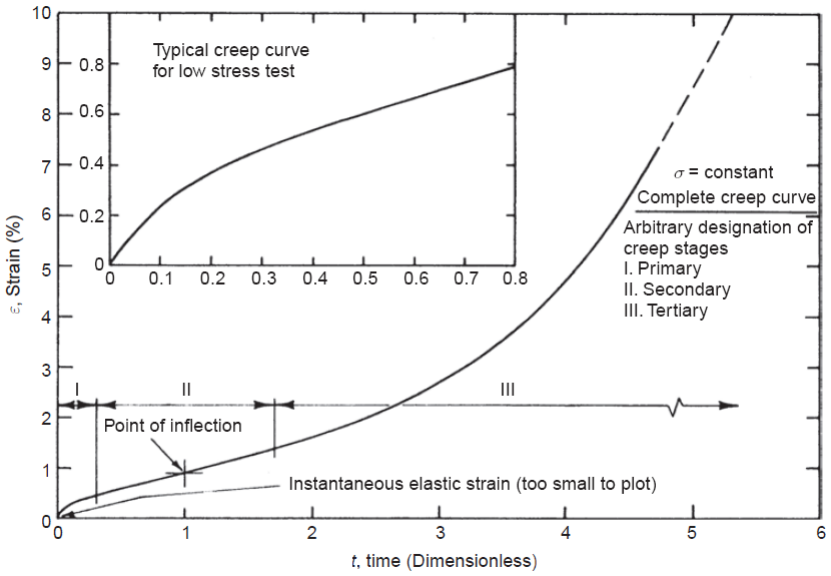

Figure 8: Typical creep curve of isotropic granular ice at constant stress [21]

At the beginning of the first stage, there is an elastic strain ϵ_e, following Hooke's law. The molecules are only pushed together without damage [20]. This is followed by primary or transient creep where grains whose orientation promotes basal sliding, get deformed first. Initial dislocations form, but the creep rate decreases continuously since the grains which are still differently oriented, impede each other. This primary creep occurs up to about 1% of the strain. If the load is removed during this stage, the strain includes a time-dependent recoverable strain or delayed elastic strain [30]. At the stage II of secondary creep, the creep rate reaches a minimum which can be defined in the range of strain of about 1 to 2% and appears to remain constant which indicates a nearly steady-state condition. Secondary creep is located in the transition between the decelerating primary creep and tertiary creep functioned accelerating [16]. When passing the 10% strain mark, a steady state can be reached when cracking does not occur. In that the case, the increasing of creep rate after stage II effects the development of preferred crystal orientation (textures or fabrics) and dynamic recrystallization [4]. During the last stage denoted as tertiary creep, the steady state implies stable textures and the equilibrium between hardening which means the development of internal stresses and softening related to recovery and recrystallization processes [30]. It has to be noted, that relatively high temperature and the development of recrystallization textures are needed for such behavior [16], [4]. But a plastic strain of 10% is far too small to achieve crystals slip. Most of the textures in polar ice sheets (where plastic strain can exceed unity) are induced by slip since recrystallization is not very active at relatively low temperatures [30]. For some of the deformation modes grain size is a factor, but only within very finely grained material. Therefore refinement increases the steady-state creep rate [17].

In the case of tests with a constant strain rate like common in ice engineering, they are performed with short-term transient loading till failure. Thereby the strain rates are mostly higher than $10^{-7}s^{-1}$ and the deformation occurs with the formation of cracks. Jones et al (2003) conducted some experiments below the ductile-to-brittle transition at a strain rate of $10^{-7}s^{-1}$ from which the following Figure 9 emerged. It shows a typical stress–strain curve of the measured data.

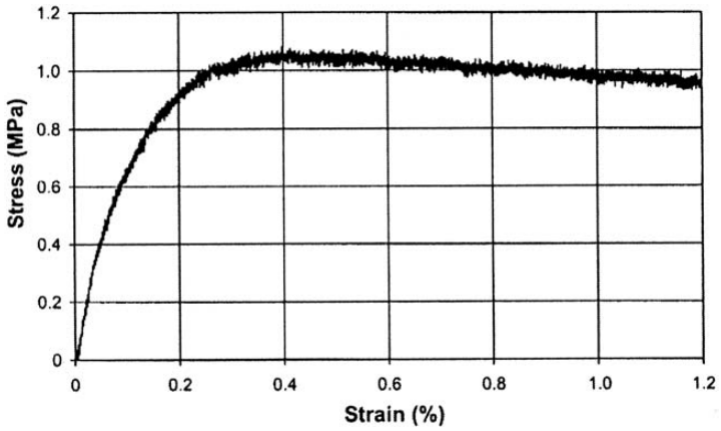

Figure 9: Typical stress strain curve for a sample tested at -10 °C and $10^{-7}s^{-1}$ [30]

The slope of the curve $\sigma(\epsilon)$ at the origin is lower than the true Young's modulus at low strain rates since the material of the specimen is plastic from the beginning [30]. After reaching the peak at a strain of about 0.4%, there is a small decrease of stress. According to Schulson (2009) [30] this softening is associated with dynamic recrystallization.

From Mellor (1980) [21], the peak stress can be noticed in a range of strain between 0.2 and 1.5%. Some researches have proven that the constant stress test (creep) and the constant strain-rate test (strength) give pretty much the same information but only in regard of to ductile behavior. Due to the fact that cracking cannot be excluded in such tests, the comparison is limited to a small range of strain rates. After Michel (1978) [23], the value of the activation energy determined from the peak stress is about 80 kJ/mole for strain rates between 10^{-8} and $10^{-7}s^{-1}$ which is close to the one determined for secondary creep.

3.3 The Mechanism of Brittle Failure under Compression

Brittle behavior has particularly more significance for the design of engineered structures challenging ice in polar regions. Due to the encounter speed in ice-structure interactions brittle failure is the most common case and states the limiting loads. Schulson (1999) [29] describes brittle failure under compressive load as a multi-step process. The beginning can be found in the nucleation of cracks at grain boundaries at applied stresses around one-quarter to one-third of the failure stress [29]. This continues with a progressive and generally uniform increase in the crack density throughout the specimen when

the load rises. The termination occurs near the peak of the stress-strain curve through sudden formations of one or more macroscopic shear faults after shortening less than about 0.5% [30].

When considering brittle failure two parts have to be distinguished: confined and unconfined ice. In ice-structure interactions compressive failure often occurs under a multiaxial state of stress. Ice within the contact zone is compressed not only along the direction of impact, but also in orthogonal directions, due to constraints by material around. This kind of confinement effects biaxial and triaxial stress states, which play a great role on the strength of the ice and on its mode of failure [9]. Confinement has two effects: firstly, it reduces sliding because it lessens the effective shear stress and secondly, it lowers the stress intensity factor K_I which is a measuring parameter for fracture toughness and describes how close a loaded crack is to propagation. Based on these affects, higher applied stresses are required to start the mechanism [7]. There are two kinds of shear fault under triaxial loading which depend on the degree of cofinement: plastic or high-confinment-fault and coulombic or low-confinement-fault [36] which are shown in Figure 10.

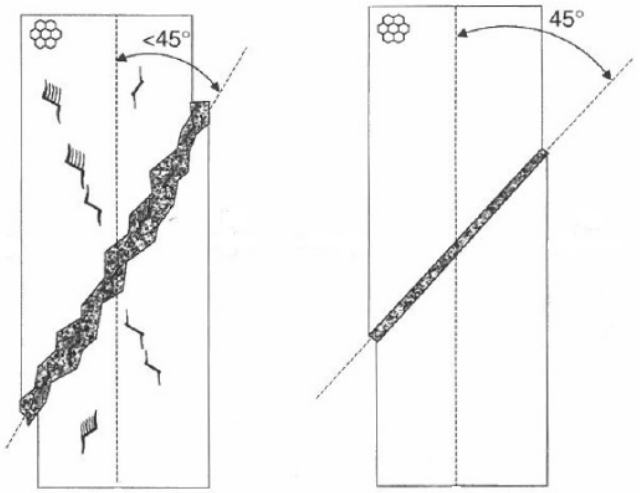

Figure 10: Schematic sketch of compressive shear faults. Coulombic fault (left) and plastic fault (right) under triaxial confinement [30]

Thereby plastic faults are inclined by 45° and coulombic faults by 25 - 30° to the direction of the principal stress [30]. In the case of unconfined ice axial splitting can occur.

In Figure 11 Renshaw et al. (2014) [27] show the applied strain rate as a function of the confinement ratio for granular S2 and columnar ice. The solid lines in the graph show the observations for $T = -10$ °C, while the dashed lines represent the results for $T = -40$ °C. The most notable discrepancy is that the critical applied strain rate at which ductile deformation transitions to P-faulting in columnar ice, is about a factor of four lower than the one observed for granular ice.

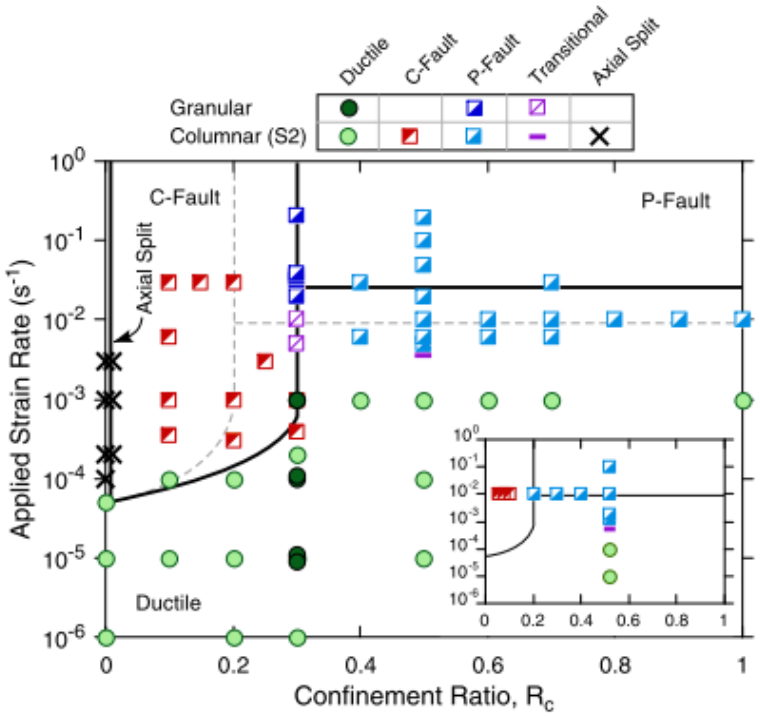

Figure 11: Modes of failure as a function of the confinement ratio and the applied strain rate [27]

To get deeper information about the mechanisms, Schulson (1999) [29], conducted some research on coarsely grained columnar fresh-water ice with a grain size of about 10 mm, loaded biaxial across the columns under a moderate degree of confinement (R = 0.1) at a temperature of –10°C and a strain rate of $5 \cdot 10^{-3} s^{-1}$. His observations are shown in Figure 12. Therein the long axis of the grains is perpendicular to the page. Figure 12(a) illustrates a typical terminal shear fault under compression as already mentioned, where the fault runs from the upper right to the lower left while Figure 12(b) visualizes a related thin section.

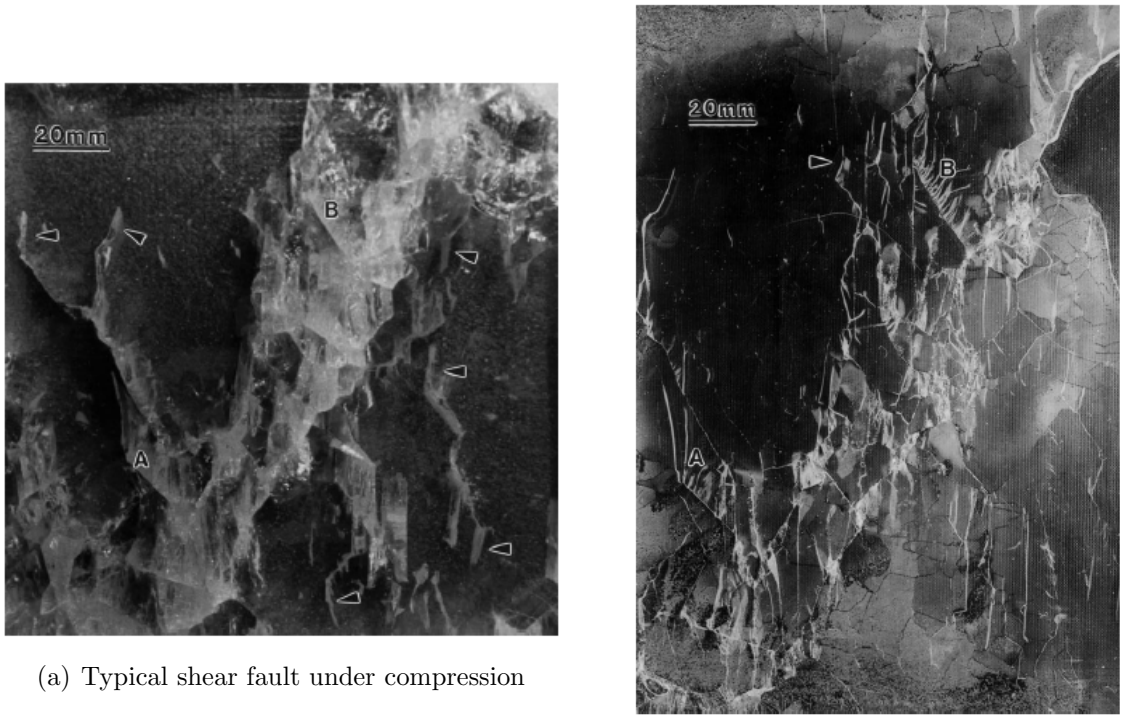

(a) Typical shear fault under compression

(b) Thin section of the shear fault

Figure 12: Compressive shear fault in columnar-grained ice

Out of this the following observations and conclusions are worth mentioning:

- The fault is a zone of damage with a size of about 2–3 grain diameters. And it is inclined by 26° to the principal stress which is introduced vertically.
- There are wing-cracks denoted with an arrow which are distributed across the whole field of damage. They originate from the tips of intergranular parent cracks, which are inclined by about 45° to the direction of the principal stress.
- The fault has zigzag edges, from which one can conclude that wing cracks are an element in its structure.
- There are milky parts like A and B in Figure 12(a) originated from one side of some parent-inclined cracks. Taking a closer look these areas are closely spaced secondary cracks of about 0.5 of the grain diameter so-called splay cracks which can be recognized in the thin section in Figure 12(b) [29].

By the means of previous experiments and analyses it could be ascertained that the parent cracks nucleate through grain boundary sliding [8]. Frictional sliding of these parent cracks triggers the growth of wing cracks. After Schulson et al (1999) [29] the secondary cracks or splay cracks initiate from Hertzian contact stresses across the parent crack faces. Afterwards they spread within a tensile field, which is emerged by nonuniform

displacements across the sliding crack in the most cases. Schulson holds the view that splay cracks are critical features in initiating the fault, cause they create sets of closely spaced microcolumns which are fixed on one end and free on the other. When the free end gets in contact with the sliding crack, a momentum results that causes the columns to bend and break like seen in Figure 13 (a). M and P are the induced momentum and axial load of the microcolumn while τ and σ_n stand for the shear stress and normal stress, that is acting on the microcolumn. ψ is the inclination of the parent crack.

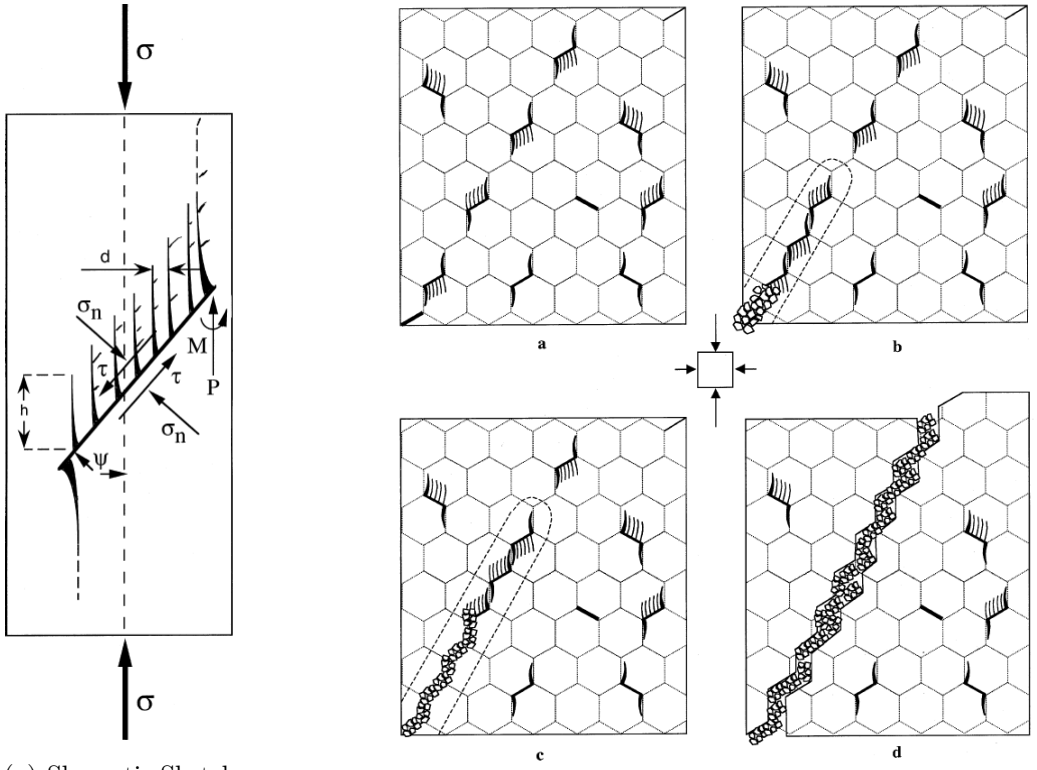

(a) Shematic Sketch of the com-crack-mechanism

(b) Development of a compressive shear fault through the implied hexagonal microstructure

Figure 13: Schematic development of a compressive shear fault [29]

As a result the failure of these microcolumns under frictional shear loading could be responsible for the fault. Thereby the microcolumns located near the surface probably break first, cause of less constraints there. Afterwards they grow along a band of reduced shear strength that emerges due to splay cracks that have been formed before fault initiation and additionally fresh splay cracks that are created just ahead of the progressing fault front like seen in Figure 13 (b). This continues rapidly till the front crosses the section and finally causes the fault [29].
Also in the case of granular ice, the course of events described above can be applied [30]. However, the shape of the grains plays the crucial role here which influences the orientation of the wing cracks and so the deformation of the ice body. Since the plane of the crack is randomly oriented within the zone of the applied stress, lateral displacement is

symmetric about the loading direction which effects macroscopically three-dimensional inelastic deformation [30]. Following from this, axial splitting can occur on any plane oriented parallel to the loading direction. When looking again on columnar grown ice that is loaded uniaxially across the columns, the wing-crack plane is constrained due to its microstructure and is oriented more or less parallel to the long axis of the columns. This leads to two-dimensional inelastic deformation which in turn causes that axial splits form only on macroscopic planes, parallel to the columns [29].

Back to columnar ice, both the primary and the secondary wing cracks are parallel to the long axis of the grains. The primary cracks initiate either near or on the free surface and then deepen inward along the grain boundaries. The secondary cracks also deepen by growing along the direction of load. In laboratory test, the length of columnar grains within a specimen is often greater than the thickness. This means that cracks can only shield each other slightly in regard along the columns [30]. This is different in granular ice where cracks do shield each other. The nucleation of primary cracks often happens on randomly oriented grain boundaries but they do not grow in depth cause secondary cracks sprout from their tips. Wing-cracks can now grow both, along the direction of loading and around the parent cracks and then move into depth inward and outward on approximately the same plane that is parallel to the loading direction [30]. In granular ice, this is hardly recognizable.
As a conclusion it can be said that brittle compressive failure is a process which begins in an early state of deformation as the first primary cracks nucleate. As the load rises this continues and new cracks nucleate while older ones already develop wings that grow and interact. When the amount of crack interactions with each other and with free surfaces exceed a limit, the specimen suddenly collapses and terminates the process.

3.4 The Mechanism of Ductile-Brittle Transition under Compression

The ductile-brittle transition area is besides brittle behavior also of particular importance for the engineering of ice going structures. When looking again at Figure 7, it can be seen that the transition between II and III is characterized by the highest compressive strength of the ice which can be seen as the maximum forces induced by a floating ice cover when pushing against the sides of a structure [3]. Schulson (1999) [29] describes the ductile-brittle transition as a competition between stress relaxation and stress build-up at crack tips. These crack-tip stresses relax through creep deformation at intermediate rates. As a consequence the stress intensity factor K_I never reaches the critical level, at neither the tips of wing cracks nor splay cracks. In contrast to that, stress build up dominates at high rates of deformation, and the K_I factor quickly reaches the critical level K_{IC}. When either the stress relaxation and the stress build-up are in balance, the transition emerges. By the means of frictional sliding-crack mechanics from Ashby-Hallam and crack-tip creep after Riedel-Rice, Schulson (1999) [29] modeled this process to express the transition strain rate like seen in equation (1). He assumes that cracks

propagate when the size of the crack-tip creep zone falls below a small fraction f of the crack length. The formula of the transition strain rate contains the independently measurable parameters of the fracture resistance (K_{IC},), the creep constant B, ($\dot{\epsilon} \propto B\sigma^{1/m}$) friction ($\mu$), and the crack length (D).

$$\dot{\epsilon}_{II,III} = \frac{BK_{IC}^3}{fD^{1.5}\{[1+\mu^2]^{0.5} - \mu - R[\mu + (1+\mu^2)^{0.5}]\}} \tag{1}$$

To review the relationship of formula (1) Schulson et al (1999) [29] performed some experiments and shows that the model correctly captures the effects of crack size, confinement, and brine pores. Additionally the model predicts a transition strain rate of $10^{-3}s^{-1}$, which is close to that observed for the conditions of Figure 7. The relation in equation (1) also shows that the transition strain rate is only slightly dependent of temperature cause of the effects of temperature on friction and creep. At least over the range of –40°C to –3°C which is also confirm with the observations of his experiments.

The influence of the grain size on the transition strain rate can be graphically clarified like shown in Figure 14. The theoretical line results from the equation above.

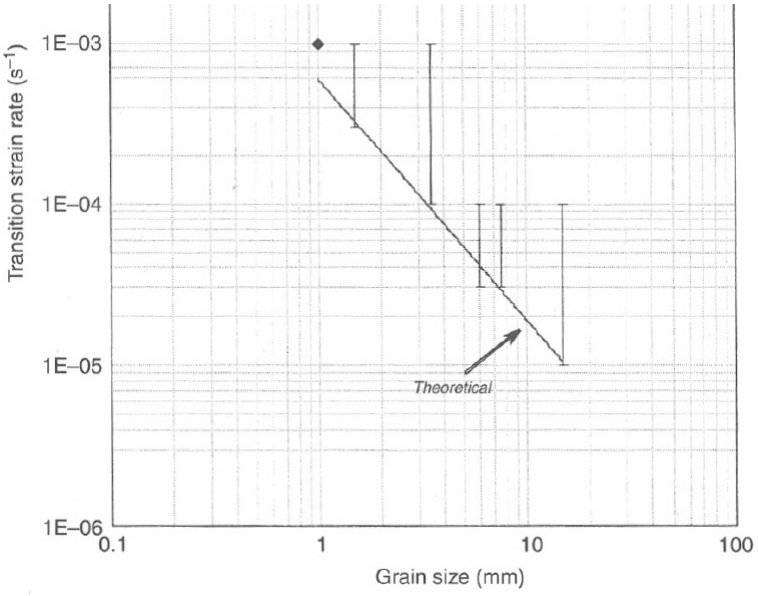

Figure 14: Ductile-to-brittle transition strain rate over grain size for unconfined, columnar fresh water ice [30]

The bars represent the results of performed compression tests with unconfined, columnar grown fresh water ice at -10°C. If a specimen gets compressed at a rate which is equal or lower than the one at the bottom of the bar, it behaves ductile. And on the other side, if a specimen gets compressed at a rate which is equal or higher than the top of the bar, it behaves brittle [30]. Different from other figures, here the transition range is only very small dependent on the grain size.

4 Experimental Conduction and Analysis

In chapter (2) we got some insights into the internal structure of the ice and its formation. Some questions about the mechanisms under compressive load have been clarified in chapter (3), although not all could have been resolved yet. To gather further information in this regard the second part of this thesis outlines a description and analysis of a number of conducted compression tests of cylindrical specimen composed of laboratory-made freshwater ice, manufactured with three different methods especially to gain information about the compressive strength. Previous pilot tests performed at the institute, show divergent results and could not be used scientifically. In this regard the ice cylinders were produced in a modified deep freezer, where columnar ice was formed out of distilled water. The compression tests were carried out uncooled at ambient temperature which is not suggestive. Due to the resulting scatter range, more reproducible samples with only slight deviations in regard of strength values are of special interest in the scope of this thesis. Therefore a newly installed test setup in a separate cooled container is used. To improve the internal grain structure and especially to obtain a homogeneous ice sample over the entire length, two different types of crushed ice are utilized and compared. In order to draw a comparison with the previous researches, a series of tests with columnar ice is also analyzed within the new experimental setup. In addition to the investigation of the strength parameters, the failure modes of the tests are also determined. Furthermore, the speed dependence of the compression strength is shown by means of one selected manufacturing method with the most valuable results in regard of strength.

At first glance compressive strength seems to be one of the most simple measurements to apply. But good values require great care in experimental procedure. Consequently, attention must be paid to the following number of influencing factors that concern either the sample preparation as well as the alignment of loading [31]:

- Temperature
- Water ingredients
- Preparation techniques
- Growth direction
- Grain size
- Crystal orientation

And additional dependencies of the simple compression tests:

- Sample size and shape
- Parallelism of specimen ends
- Stiffness of the test machine
- Confinement conditions
- Loading direction
- Rate of loading

The following sections take up these points and show all details of the specimen generation, the difference of their properties, affected by the three production processes as well as the experimental set-up and the configuration of the test parameters.

4.1 Specimen Production

First of all we focus on the three different ways of production of the ice samples subdivided into two granular types out of different crushed ice pieces mixed with distilled water and one columnar type composed of pure distilled water.
The granular crushed ice samples, carried out within this scope, are generated in a modified reefer container at a freezing temperature of -10 °C. The specimen are emerged in special cylindrical molds consisting of a PVC tube with a length of 200 mm and an internal diameter of 99,4 mm. The walls thickness amounts to 10 mm. This tube is glued on a well thermo conductive, quadratic metal plate with an edge length of 135 mm and a thickness of 2 mm. For the freezing process, this construction is placed on the bottom of the reefer container. In order to ensure that the freezing process takes place unilaterally from the bottom up, the specimen holders are covered with wooden and Styrofoam lids after being filled.

The distinction of the granular ice types, is rooted in the manufacturing process of the crushed ice pieces. On the one hand commercial crushed ice, produced industrially out of fresh water from the tap and on the other hand self-made crushed ice out of distilled water is being utilized. The latter is made of big ice blocks that are formed in a trough in which the water slowly circulates during the freezing process by the means of small water pumps at the bottom. As a result, the generated ice contains almost no visible air inclusions. After solidification the ice block is shred with a hammer or better a crushing machine first. Since these fragments have different sizes, they are selected using two sieves with different mesh openings. In this way, two test series have emerged, one with 4-6 mm fragments and the other with 6-11 mm fragments. This process creates a mixture of various small crushed ice fragments of similar size. The aim of this process is to generate ice samples with a uniformly granular polycrystalline texture. The other type of granular specimen out of commercial ice pieces are also crushed and sieved with a mesh opening of 4 and 6 mm for one test series for better comparison. For all other test series, the commercial crushed ice pieces are used directly without further treatment.

After the manufacturing process of the crushed ice particles, they are dosed with distilled water of ambient temperature. This type of water is used, since the controlling of the composition of fresh water from the tap or sea water is difficult. Additionally, it should provide a greater compressive strength than fresh or sea water due to a lesser amount of weakening impurities [2]. This is favorable for the experiments, because maximum strength values are being investigated. In doing so, the distilled water is stratified alternately with crushed ice pieces into the molds. Meanwhile stirring increases a consistent wetting of the ice pieces. At the end the ice-water compound is stamped with a handily rammer to compress the mixture and force the water into the interstices between the crushed ice pieces which will reduce the amount of air inclusions. After filling, the samples are covered and remained in the reefer container for about 18 hours till they are consistently frozen. After this period, the tubes with its fixed ice cylinders are slightly defrozen at ambient temperature until the ice cylinders can be pressed out of the molds.

Afterwards, the samples are stored at -10 °C in the refrigerated container until further processing.

For comparison to further researches, another series of tests with pure distilled water is prepared. This takes place in an extra-modified deep freezer at -60 °C like shown in Figure 15.

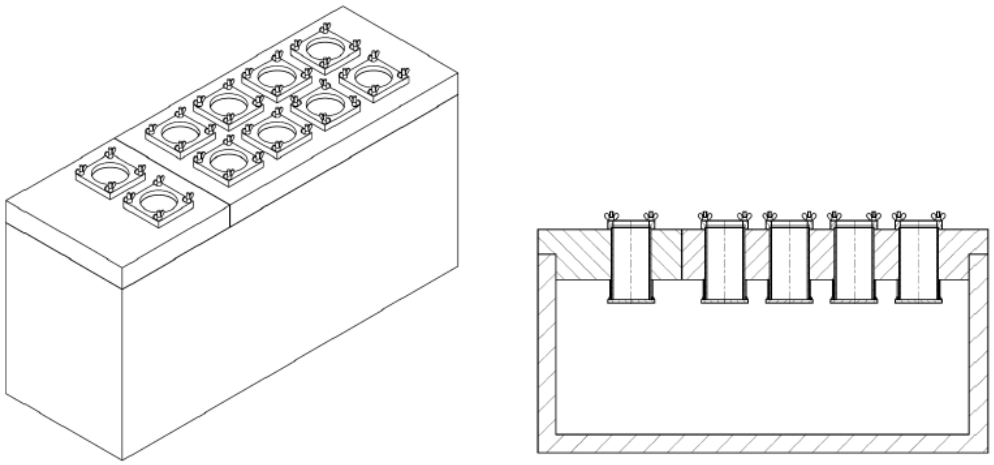

(a) Isometric view (b) Sectional view

Figure 15: Isometric and sectional view of the deep freezer [6]

Its chest is closed with a thick styrodur block which contains openings for the sample holders, consisting of the same PVC tubes as described above. They are screwed tightly with a covered steel plate into the styrodur block. Thus, the bottom of the sample is in contact with the prevailing temperature within the freezer, while the top is outside the block at ambient temperature. This ensures that the ice can freeze unidirectional, starting from the bottom. After a freezing time of 48 hours, the samples can be removed again.

After all samples are defrozen, they are sawed to the desired length using a band saw. It should be noted that the samples are trimmed at the top and bottom, so that parallelism between the ends is ensured. After the saw cuts, the samples have a length of 175 mm, thus resulting in a length to diameter ratio of 1,76. Until the compression tests, the specimen are again stored in polystyrene boxes at -10 °C in the reefer container. In the further course, the samples out of self-made crushed ice are shortened with SMCI and the samples from commercial crushed ice with CCI and the ones out of the deep freezer with DF. The additional designation DW stands for distilled water.

The visually conspicuous differences between the two crushed ice varieties and the deep freezer specimen are reflected in the grain structure and the unintentional air entrapment. For this purpose we will look at one exemplary specimen for each manufacturing process which are shown in Figure 16.

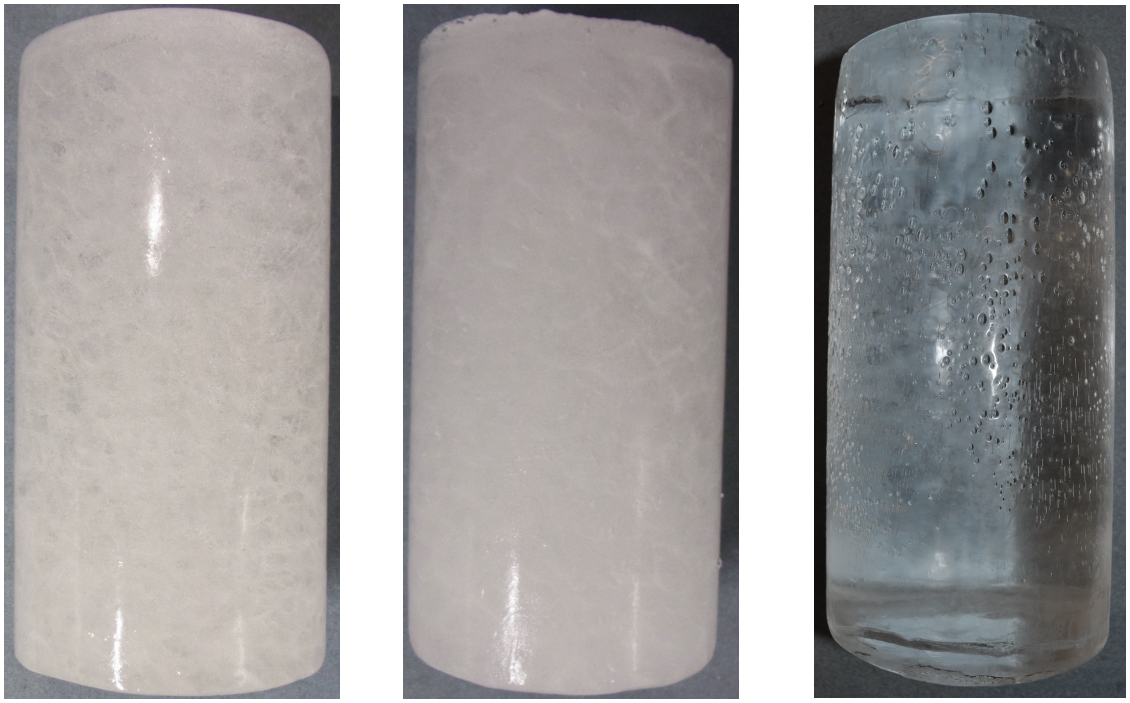

(a) SMCI+DW20 (b) CCI+DW20 (c) DF_DW20

Figure 16: Typical specimen of each test series

Both of the crushed ice specimen in Figure 16 (a) and (b) are opaque and only the silhouettes of the crushed ice pieces can be spotted. It has to be mentioned that the SMCI+DW20 specimen has some more clear areas than the specimen out of commercial crushed ice. This is caused by the industrial production process where a large quantity of air is already enclosed in the ice during the freezing process so that the crushed ice pieces appear opaque. The sample from the deep freezer, on the left is very clear, it is only disturbed by some air inclusions distributed over the shell of the sample. Cause for that are air bubbles accumulating on the inner shell of the PVC tube after filling that get enclosed in the ice during the freezing process.

To reflect the internal structure of the ice samples, 1 mm thin sections are cut of one sample of each manufacturing process by using a band saw. By the means of two crossed polarization filters the several grains of the structure can be displayed by different light refractions when exposed. The next Figures (17 till 21) show exemplary one thin section polarized and unfiltered for the three manufacturing methods and their offsets with different sieved crushed ice pieces.

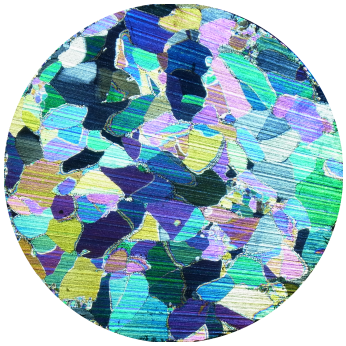

(a) Thin sectin polarized

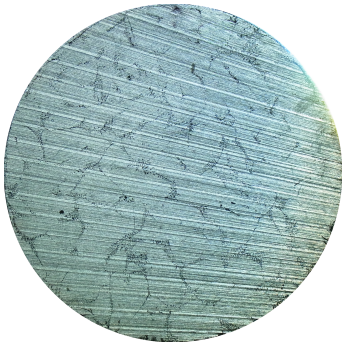

(b) Thin section unfiltered

Figure 17: Typical granular thin section of self-made crushed ice sieved with mesh openings of 6 and 11 mm and mixed with distilled water (SMCI+DW20_6-11)

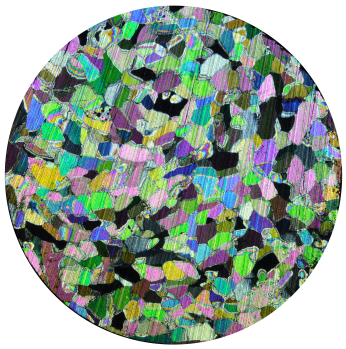

(a) Thin section polarized

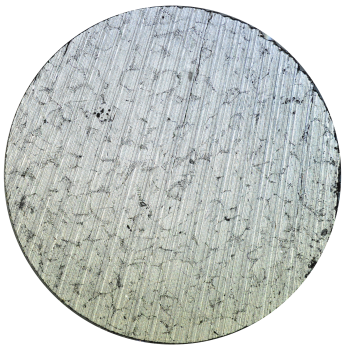

(b) Thin section unfiltered

Figure 18: Typical granular thin section of self-made crushed ice sieved with mesh openings of 4 and 6 mm and mixed with distilled water (SMCI+DW20_4-6)

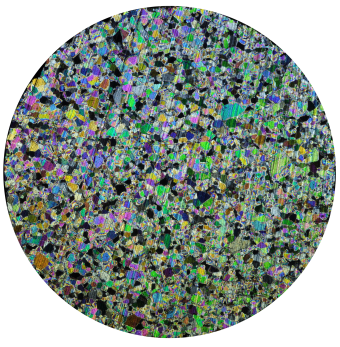

(a) Thin section polarized

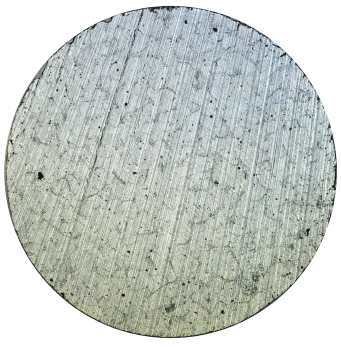

(b) Thin section unfiltered

Figure 19: Typical granular thin section of commercial crushed ice sieved with mesh openings of 4 and 6 mm and mixed with distilled water (CCI+DW20_4-6)

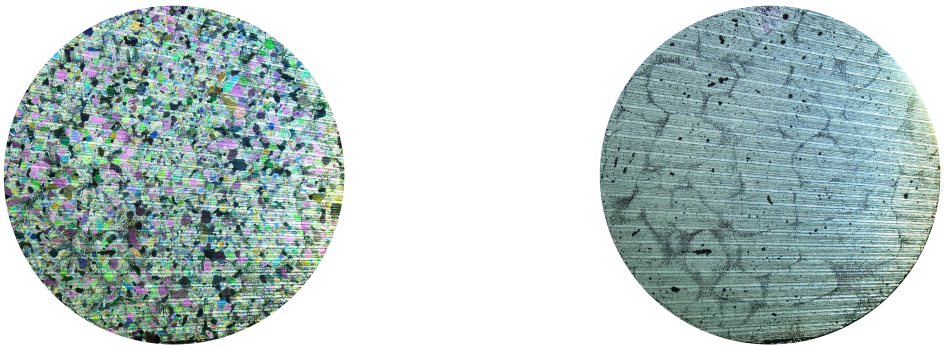

(a) Thin section polarized (b) Thin section unfiltered

Figure 20: Typical granular thin section of unsieved commercial crushed ice mixed with distilled water (CCI+DW20)

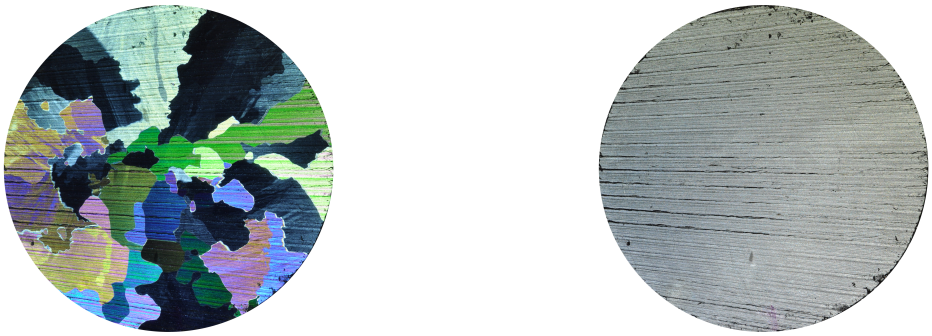

(a) Thin section polarized (b) Thin section unfiltered

Figure 21: Typical thin section of columnar grown ice of pure distilled water out of the deep freezer (DF_DW20)

The first noticeable point to see, is that the thin sections of the crushed ice specimen differ significantly in regard of the grain size. The thin sections of the SMCI_4-6+DW20 test series has obvious greater grains than the one of the CCI+DW20_4-6 test series although they consist of same sized crushed ice fragments. This takes place because the self-made ice is generated in a big trough where the ice could grow from a large free water surface effected in great grain like common in natural calm water bodies. Thus, one crushed ice piece often contains only one grain. The high color spectrum of the consistent angular grain shapes is rooted in randomly oriented c-axes. This is the same case as in the CCI+DW20 thin sections but the grains and their boundary are hardly recognizable as they often pass into one another. Further conspicuous features are the air inclusions as already seen in Figure 16, which can be descried by means of the black spots in the unfiltered thin sections. On the one hand they are accumulated at the boundaries of the crushed ice pieces, which are present in both manufacturing methods and on the other hand they are scattered within the crushed ice pieces. In the latter case the samples out of commercial crushed ice, have larger amount of air inclusions

due to the manufacturing process of the crushed ice pieces as already mentioned. In comparison the grains of the deep freezer samples are significantly larger. In the case of columnar ice, only the grains with favorably oriented c-axes can grow into depth, so that the number of grains changes with progressive growth. Air pockets are only slightly present here on the perimeter of the specimen.

4.2 Evaluation of Grain Size

For a better understanding of the mechanical behavior of the ice samples and a possible comparison among each other, the inner structure has to be considered. In this context the grain size is of particular interest which can be estimated with a standardized test method called circular process [5] which is especially used for fine grained structures like present in the crushed ice specimens. Therefor the photographs of the thin sections are used and graphically evaluated by counting grains in several randomly positioned circular areas of known size which are drawn into the photo. In one circle at least 50 grains should be included. Firstly the number N_1 of the grains located in the circle and the number N_2 of the grains on the perimeter, are counted. The total number N is computed as following:

$$N = N_1 + \frac{N_2}{2} \tag{2}$$

The mean grain area a is determined by dividing the circular area A_0 by the total number of grains N:

$$a = \frac{A_0}{N} \tag{3}$$

From the mean grain area, we can finally determine an equivalent diameter of one grain.

$$d = \sqrt{\frac{4 \cdot a}{\pi}} \tag{4}$$

The resulting outcomes for the different manufacturing methods (and their extensions) are listed in Table 1.

Table 1: Results of the grain size analysis

Test Series	A_0 [mm^2]	N_1 [-]	N_2 [-]	N [-]	a [mm^2]	d [mm]
SMCI+DW20_6-11(_1)	232,08	6	10	11	21,10	5,18
	232,08	2	10	7	33,15	6,50
	232,08	2	10	7	33,15	6,50
Average					29,10	6,06
SMCI+DW20_4-6(_1)	497,84	29	20	39	12,77	4,03
	497,84	24	24	36	13,83	4,20
	497,84	26	22	37	13,46	4,14
Average					13,35	4,12
CCI+DW20_4-6(_1)	134,59	66	31	81,5	1,65	1,45
	134,59	62	28	76	1,77	1,50
	134,59	61	29	75,5	1,78	1,51
Average					1,73	1,49
CCI+DW20(_1)	235,06	89	29	103,5	2,27	1,70
	235,06	83	36	101	2,33	1,72
	235,06	98	36	116	2,03	1,61
Average					2,21	1,68
DF_DW20(_1)	1579,14	17	15	24,5	64,45	9,06
	1579,14	11	12	17	92,89	10,88
	1579,14	10	17	18,5	85,36	10,43
Average					80,90	10,12

4.3 Experimental Setup

After the specimens have been produced and the first optical observations have been recorded, simple compression test are used to evaluate the mechanical behavior of the ice samples. In contrast to previous pilot tests, now the compressive tests are carried out in a cooled environment for the first time like shown in Figure 22. Therefore a specially designed cooling chamber is used. Its temperature is cooled down to -10 °C so that the samples do not melt during the experiments. The test-bed is generally composed of a hydro-pulse system PL 160 by Schenck with a maximum force of 160 kN, mounted on a frame and fixed around the chamber. A load cell and a stamp are attached to that hydraulic cylinder. When pressurized, the specimen is pushed against a rigid base plate which stands on three load cells of the type Sartorious SR 6251 with a maximal measuring of 10 t. These in turn are grounded on a solid metal table. For measuring the pressure distribution of the cylindrical base, a flexible, grid-based tactile pressure sensor is placed on top of the base plate. For this purpose the I-Scan® system by TekScan®, Inc. is used. Therefor the setup consist of a laptop connected to a VersaTek® hub which can gather several handles. For the presented experiments, only one handle and thus one sensor of the type 5101 with a nominal pressure of 3000 PSI is used. The sensor is composed of rows and columns of conductive material, separated by a semi-conductive

ink, covered inside a plastic film. When a load is applied, the electrical resistance of the ink changes. This will be measured and converted together with the force signal from the load cell as calibration, to calculate absolute pressure values.

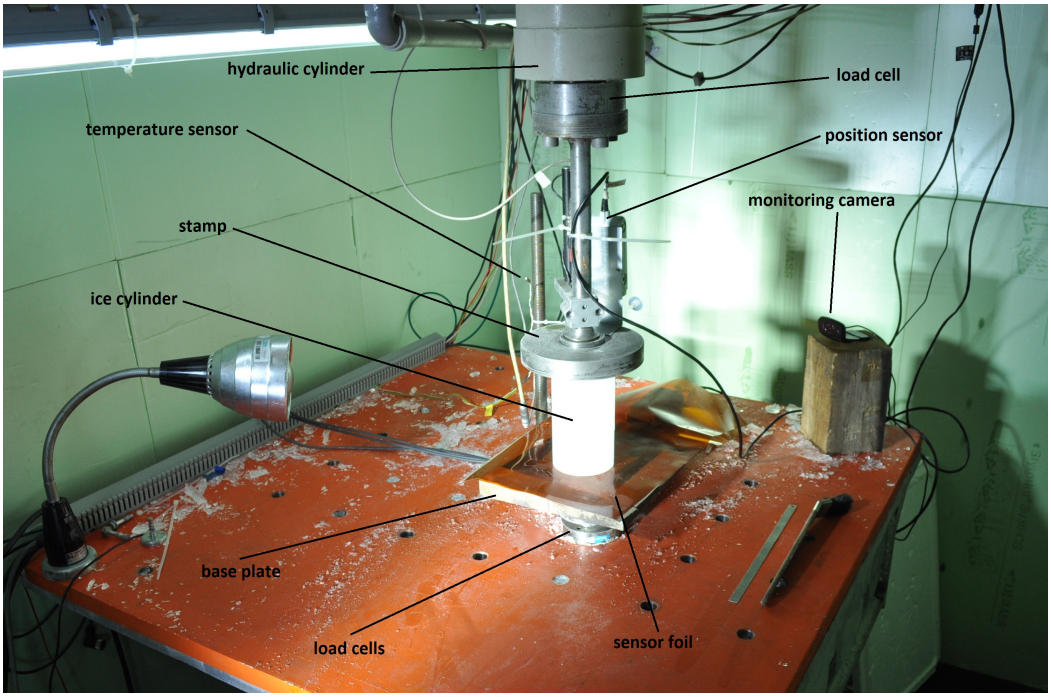

Figure 22: Test-bed for the compression tests

Before starting the test run, a specimen has to be adjusted between the baseplate with its sensor foil and the hydraulic cylinder. It is important to note how the ends of the specimen are held in the apparatus. In this case, friction is responsible for preventing the ice from expanding at the cap. This provides a restraining stress at the caps which can change the failure mode and the apparent strength [3]. After positioning, the stamp crushes the specimen against the base plate. The loads are recorded by the load cells beneath the baseplate and the cell above the stamp. The displacement of the hydraulic cylinder is also recorded by an external position sensor. The pressure distribution is noted and visualized by the means of the sensor foil. For monitoring the fracture behavior of the individual samples, a Mikrotron EoSens®mini2 high-speed camera is used, taking 700 frames per second.

4.3.1 Overview of the Compression Test Series

With the help of the newly installed experimental setup, a total number of 11 test series were carried out in the scope of this thesis. In doing so the three production methods for laboratory-made freshwater ice were compared in regard of their strength values. And on the other hand, the speed dependence of the compression strength and failure modes are evaluated. An overview of the compositions and the test conditions are summarized in Table 2.

Table 2: Outline of test series

Test No.	Abbreviation	Description
1	$SMCI + DW20\_6 - 11\_1$	Self-made crushed ice with 6 to 11 mm fragments, mixed with distilled water of ambient temp. and loaded with a test speed of 1 mm/s ($\dot{\epsilon} = 5,71 \cdot 10^{-3}$)
2	$SMCI + DW20\_4 - 6\_1$	Self-made crushed ice with 4 to 6 mm fragments, mixed with distilled water of ambient temp. and loaded with a test speed of 1 mm/s ($\dot{\epsilon} = 5,71 \cdot 10^{-3}$)
3	$CCI + DW20\_4 - 6\_1$	Commercial crushed ice with 4 to 6 mm fragments, mixed with distilled water of ambient temp. and loaded with a test speed of 1 mm/s ($\dot{\epsilon} = 5,71 \cdot 10^{-3}$)
4	$CCI + DW20\_1$	Unsieved commercial crushed ice, mixed with distilled water of ambient temp. and loaded with a test speed of 1 mm/s ($\dot{\epsilon} = 5,71 \cdot 10^{-3}$)
5	$CCI + DW20\_0,23$	Unsieved commercial crushed ice, mixed with distilled water of ambient temp. and loaded with a test speed of 0,23 mm/s ($\dot{\epsilon} = 1,31 \cdot 10^{-3}$)
6	$CCI + DW20\_0,165$	Unsieved commercial crushed ice, mixed with distilled water of ambient temp. and loaded with a test speed of 0,165 mm/s ($\dot{\epsilon} = 9,43 \cdot 10^{-4}$)
7	$CCI + DW20\_0,13$	Unsieved commercial crushed ice, mixed with distilled water of ambient temp. and loaded with a test speed of 0,13 mm/s ($\dot{\epsilon} = 7,43 \cdot 10^{-4}$)
8	$CCI + DW20\_0,12$	Unsieved commercial crushed ice, mixed with distilled water of ambient temp. and loaded with a test speed of 0,12 mm/s ($\dot{\epsilon} = 6,86 \cdot 10^{-4}$)
9	$CCI + DW20\_0,11$	Unsieved commercial crushed ice, mixed with distilled water of ambient temp. and loaded with a test speed of 0,11 mm/s ($\dot{\epsilon} = 6,29 \cdot 10^{-4}$)
10	$CCI + DW20\_0,1$	Unsieved commercial crushed ice, mixed with distilled water of ambient temp. and loaded with a test speed of 0,1 mm/s ($\dot{\epsilon} = 5,71 \cdot 10^{-4}$)
11	DF_DW20_1	Columnar ice generated in the deep freezer with pure distilled water of ambient temp. and loaded with a test speed of 1 mm/s ($\dot{\epsilon} = 5,71 \cdot 10^{-3}$)

The experimental strategy initially amounts to a uniform test speed of 1 mm/s in order to be able to compare the three production methods under brittle behavior. All other test series with the lower number of samples serve to determine the transitional strain rate between brittle and ductile failure. The test speed of 0,1 mm/s identifies the range of sheer ductile material behavior.

4.4 Description of the Test Course

The general course of events and the related behavior and failure mode of ice under compressive stress states depends on several factors. Different temperatures, types and orientations of the ice and various interactions of stress state and strain rate result in changes of behavior patterns. For uniaxial compression testing of cylindrical samples, Daley (2010) [3] has proposed a classification which is shown in Figure 23.

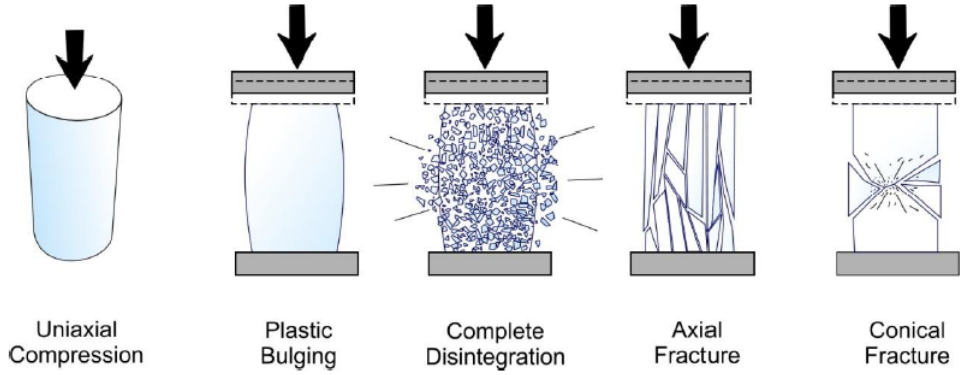

Figure 23: Common types of compressive failure in cylindrical ice samples [3]

The above-mentioned experimental speed dependency of the tests conducted in the scope of this thesis can visually be recognized in Figure 24 that plots exemplarily the relation of the hydraulic cylinder force F_{cyl} and its displacement. The red curve relates to a brittle behaviored self-made crushed ice specimen (SMCI+DW20_6-11_1) which is tested at a speed of 1 mm/s that corresponds to a strain rate of $\dot{\epsilon} = 5,71 \cdot 10^{-3}$. The blue one indicates a ductile behaviored commercial crushed ice specimen (CCI+DW20_0,11), loaded with a test speed of 0,11 mm/s ($\dot{\epsilon} = 6,29 \cdot 10^{-4}$).

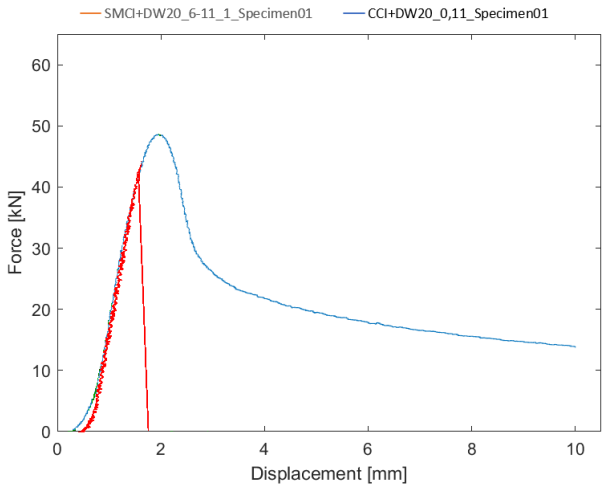

Figure 24: Force over displacement of a brittle (red) and ductile (blue) specimen

All experiments are loaded with a total displacement of 10 mm while the maximum achieved force is measured. The course of events starts after the ice specimen gets in

contact with the hydraulic stamp. The different beginnings of the curves within the plot show the minimal inaccuracy of the sawing process during the sample preparation.

In the case of brittle behavior the curve is characterized by a rise of the force till reaching the peak at which the specimen fails. The according sequence of frames of the high-speed video recording system is shown in the following Figure 25. The sample presented here is out of commercial crushed ice and loaded with 1 mm/s. This process looks the same for self-made crushed ice specimens.

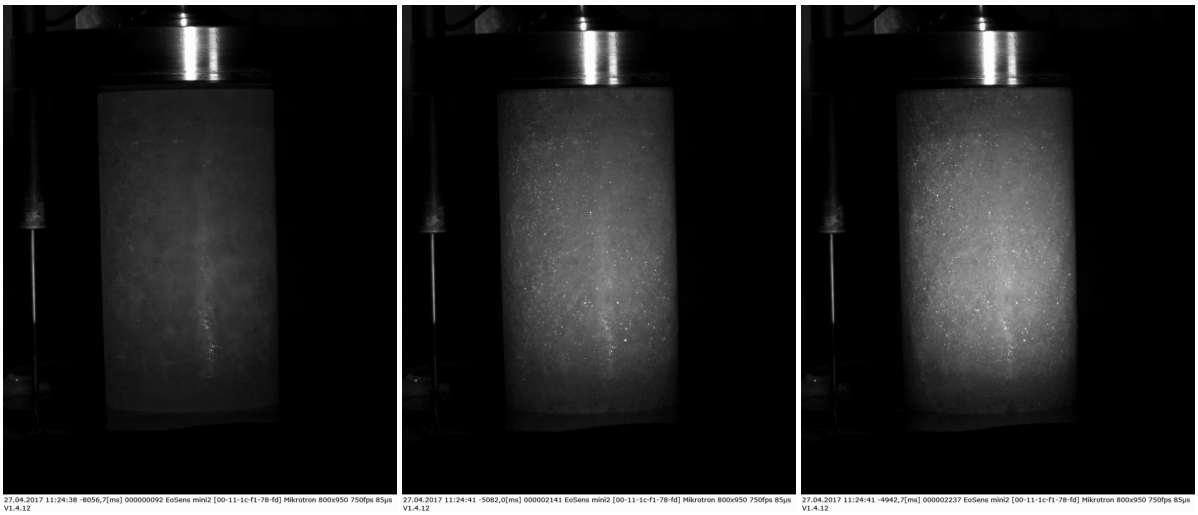

(a) Frame 01 at 0 kN (b) Frame 02 at 46,71 kN (c) Frame 03 at 52,26 kN

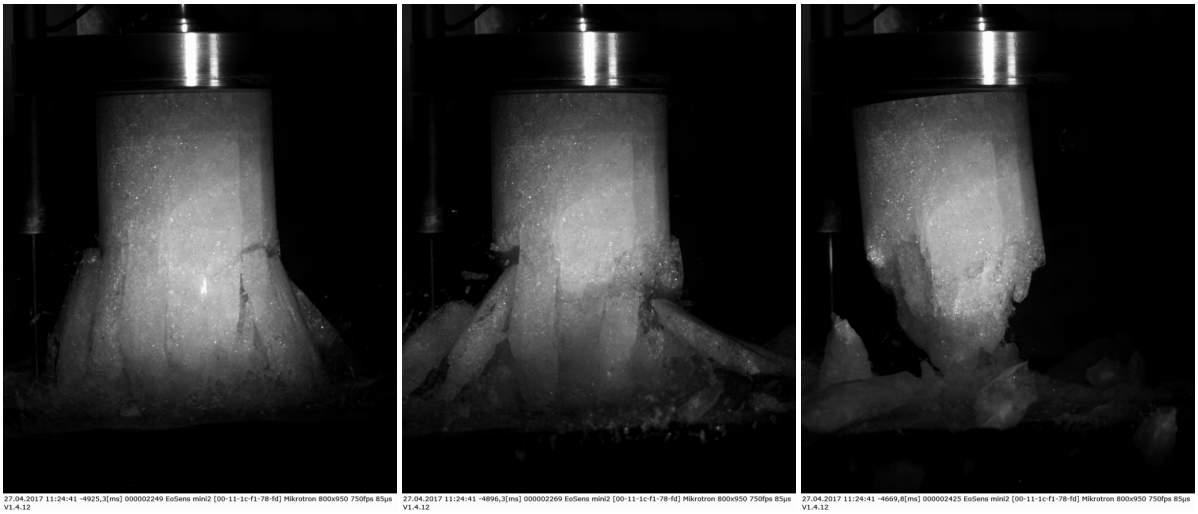

(d) Frame 04 at -6,16 kN (e) Frame 05 at -1,89 kN (f) Frame 06 at -0,88 kN

Figure 25: Sequence of brittle failure of CCI+DW20_1 specimen03

Frame one represents the sample in the unloaded state. In the following frames two to three, it can be seen that cracks uniformly occur and grow throughout the entire sample which only can be identified by the increasing light reflections within the sample. From

frame four the specimen begins to fail by a sudden release of internal energy. This stage is marked by multiple spalling of large and elongated fragments along the direction of loading which happens mainly around the lower edges of the sample. In the center of the specimen, confinement effected to the ice around hampers spalling and the typical cone-shaped fragment as presented in Figure 26 gets formed. After failure or reaching the predetermined displacement, the experiment ends.

(a) CCI+DW20_4-6_1 (b) CCI+DW20_1

Figure 26: Fragments of CCI+DW20_1 specimen after brittle behavior with conical fracture

In the case of brittle failure of the columnar grown ice samples out of the deep freezer, no sequence of the failure process could be recorded due to a problem with the high-speed camera. The process is not different from the one described above. However, most of these samples fail by axially splitting (as shown in Figure 27), which is common for unconfined material and describes an intercrystalline fracture along the grain boundaries. Thereby elongated shards break off in the direction of loading, partially over the entire length of the sample [8].

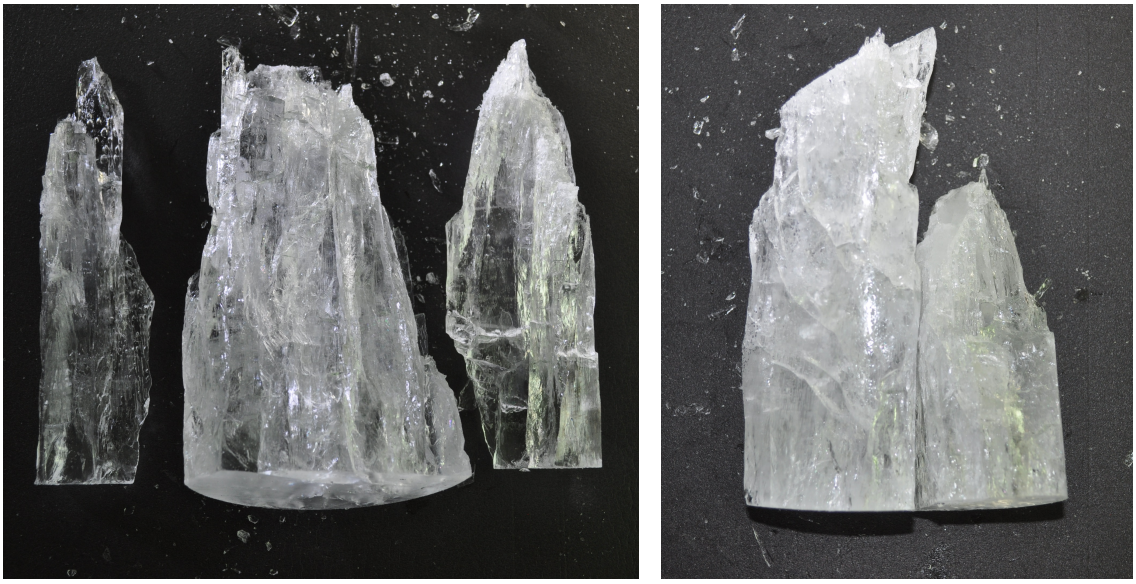

(a) DF_DW20_1 (b) DF_DW20_1

Figure 27: Fragments of DF_DW20_1 specimen after brittle behavior with axial fracture

Compared to the brittle samples, the graph of ductile specimens does not behave with an abrupt drop of force after reaching the peak, but with a steady decrease until the end of the experiment when the hydraulic cylinder reached a displacement of 10 mm. The following high-speed frames in Figure 28 belong to a specimen out of commercial crushed ice, loaded with 0,1 mm/s.

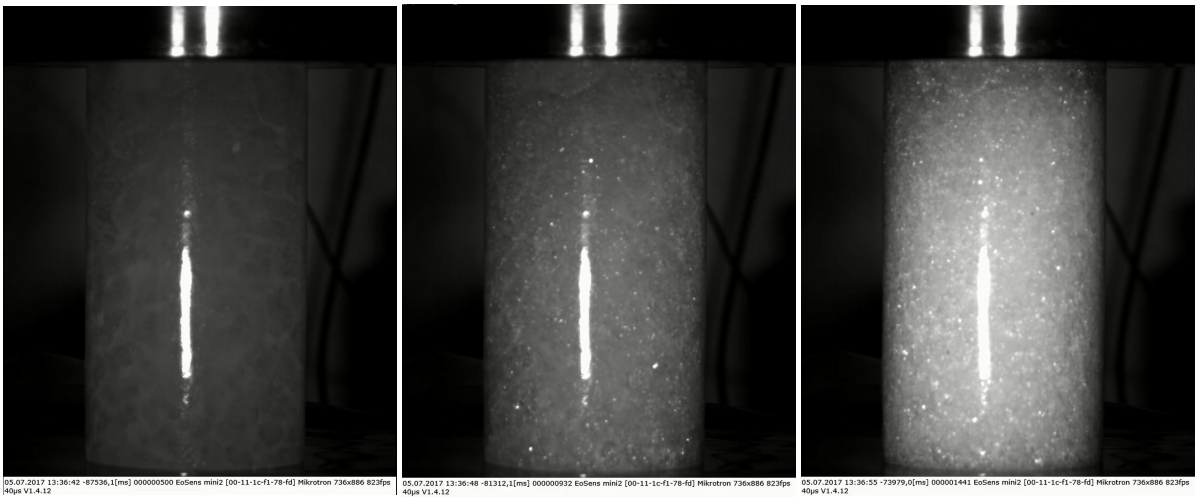

(a) Frame 01 at 5,68 kN (b) Frame 02 at 35,65 kN (c) Frame 03 at 56,41 kN

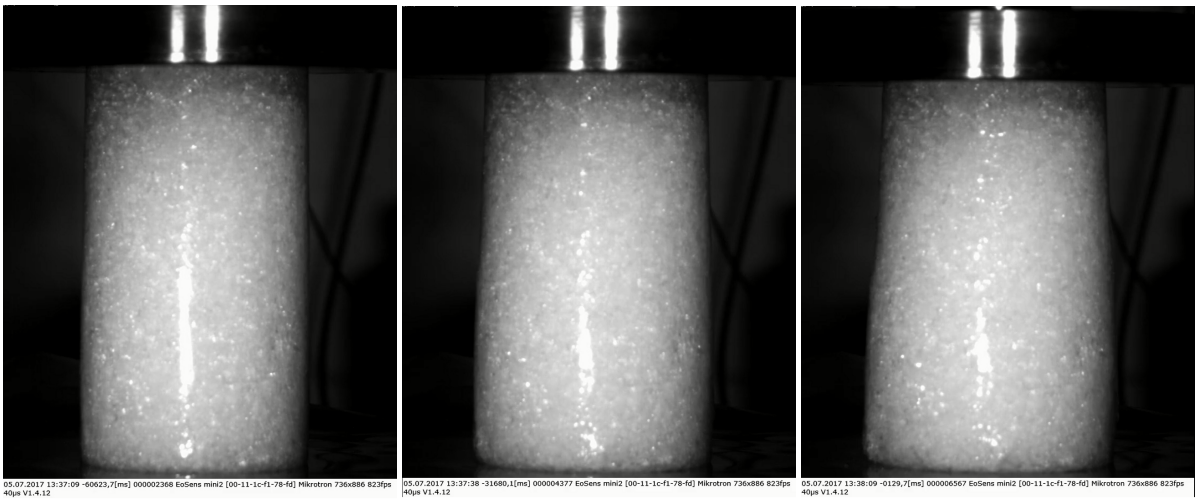

(d) Frame 04 at 26,29 kN (e) Frame 05 at 19,49 kN (f) Frame 06 at 16,21 kN

Figure 28: Sequence of ductile failure of CCI+DW20_0,1 specimen02

The increase in crack density can be recognized here again on the basis of the increasing light reflections. At the end of the test, at a strain of about 17,5%, there are no fragments arising. However, the specimens have the typical bulbous deformation in the lower part like seen in Frame 06 of Figure 28. After Daley (2010) [3] this failure mode is denoted as plastic bulging.
Specimen within the ductile-brittle transition range exhibit both, ductile and brittle behavior and are comparable with the failure processes described before.

During the tests, a flexible, grid-based tactile pressure sensor is used, which indicates the pressure distribution over the base area of the ice cylinder. This is recorded for all samples loaded at 1 mm/s like exemplarily presented in Figure 29 for a CCI+DW20_1 specimen at the peak force.

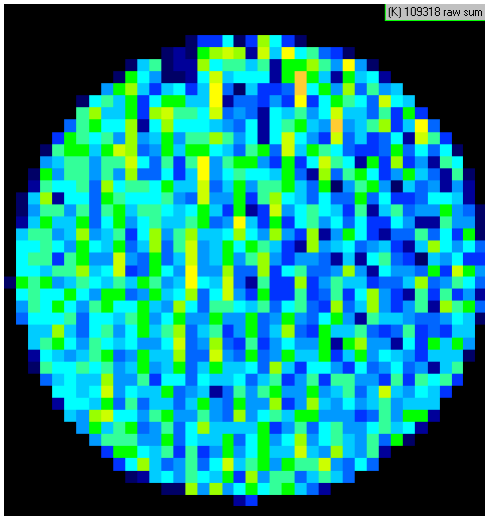

Figure 29: TekScan pressure distribution for CCI+DW20_1 specimen03 at failure force

However, no results could be observed, which would allow a connection of the pressure distribution with the material behavior or the type of failure. By comparing the recorded images, no serious differences between the individual test series can be detected. The pressure distribution of all samples starts slightly on one side, probably due to deviations of the parallelism of the specimen ends. Afterwards the pressure spreads quickly over the entire sample surface and is constantly distributed at the time of failure. Only the saw cuts stand out in color.

5 Results of the Compression Tests

This chapter lists all the results of each test series. This includes strength characteristics and failure modes of the three production methods. For this purpose, the measured temperatures as well as the hydraulic cylinder forces and the determined pressures are tabulated. In addition, the corresponding plot of the cylinder force over the displacement of the hydraulic cylinder can be found for each sample. With a small number of samples, the curves are displayed individually, otherwise summarized in one plot. In order to be able to compare the individual test series, they are statistically evaluated in a simple manner [25] [26]. In doing so the following values are considered. Firstly the arithmetic mean value which is given as:

$$\bar{x} = \frac{1}{n} \cdot \sum_{i=1}^{n} x_i \tag{5}$$

The standard deviation is defined as:

$$s = \sqrt{\frac{\sum_{i=1}^{n} {x_i}^2 - n \cdot \bar{x}^2}{n-1}} \tag{6}$$

The coefficient of variation COV, also known as relative standard deviation RSD results from the following equation:

$$COV = \frac{s}{\bar{x}} \tag{7}$$

One shortcoming of this work, is the low number of samples for some of the test series. As a consequence, a statistical statement is not possible in this case. Nevertheless, the values are given as well.

5.1 Commercial Crushed Ice

First, we have a look at the samples out of the commercial crushed ice series, starting with the one unsieved.

CCI+DW20_1

Unsieved commercial crushed ice, mixed with distilled water of ambient temp. and loaded with a ***test speed of 1 mm/s*** *($\dot{\epsilon} = 5,71 \cdot 10^{-3}$)*

The data, measured during these tests are summarized in Table 3. Due to a failed temperature sensor, no values are given here. The noted force corresponds to the force of failure. The determined pressures are relatively close to each other with a standard deviation of 0,34.

Table 3: CCI+DW20_1

Specimen No.	Temp [°C]	Force_Cyl [kN]	Pressure_Cyl [MPa]	Failure Mode
1	xx	45,55	5,85	brittle
2	xx	48,01	6,16	brittle
3	xx	52,44	6,73	brittle
4	xx	52,27	6,71	brittle
5	xx	49,33	6,33	brittle
6	xx	50,32	6,46	brittle
7	xx	46,56	5,98	brittle
Mean Value	xx	49,21	6,32	
Standard Deviation			0,34	
COV			0,05	

The following Figure 30 plots the measured forces of the hydraulic cylinder F_{cyl} over its displacement to get an insight into the behavior of the ice specimen. By reference to the abrupt drop of the force after reaching the peak, the typical course of brittle failure can be spotted for all specimen.

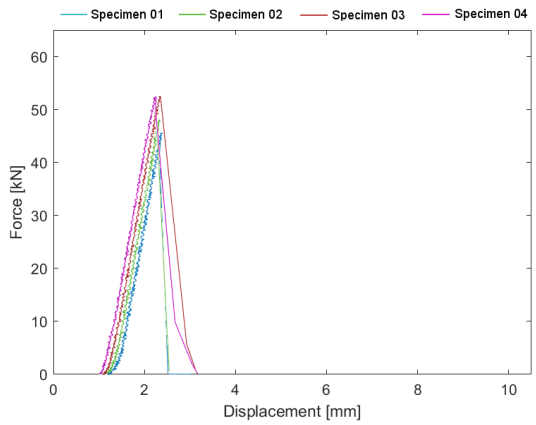

(a) CCI+DW20_1 Specimen01-04

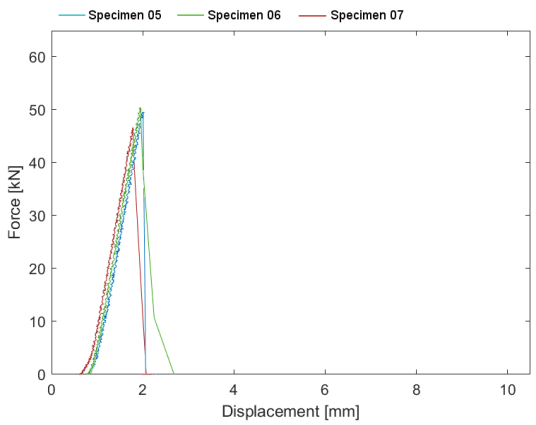

(b) CCI+DW20_1 Specimen05-07

Figure 30: CCI+DW20_1: cylinder force vs displacement

CCI+DW20_4-6_1

Commercial crushed ice with 4 to 6 mm fragments, mixed with distilled water of ambient temp. and loaded with a ***test speed of 1 mm/s*** *($\dot{\epsilon} = 5,71 \cdot 10^{-3}$)*

The next Table 4 contains the results of the sieved commercial crushed ice test series. The double sieving process with a mesh size of 4 and 6 mm reveals in a more uniform size of the inserted crushed ice pieces.

Table 4: CCI+DW20_4-6_1

Specimen No.	Temp [°C]	Force_Cyl [kN]	Pressure_Cyl [MPa]	Failure Mode
1	-9,29	52,18	6,70	brittle
2	-8,70	50,86	6,53	brittle
3	-8,71	44,66	5,73	brittle
4	-8,02	47,49	6,10	brittle
5	-7,94	44,66	5,73	brittle
Mean Value	-8,53	47,97	6,16	
Standard Deviation			0,45	
COV			0,07	

Depending on the testing speed of 1 mm/s, brittle failure patterns can be observed in this series. Despite the more homogeneous grain structure, the measured values are more scattered in comparison to the unsieved CCI series before.

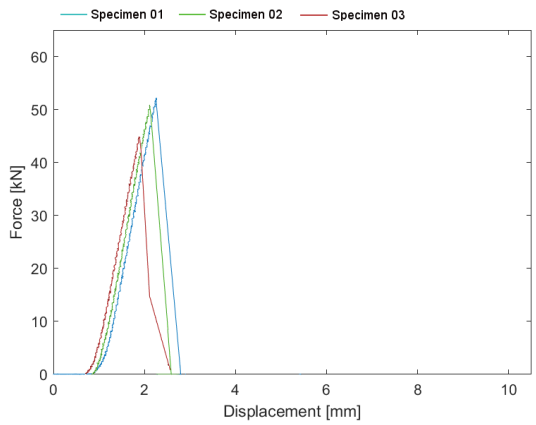

(a) CCI+DW20_4-6_1 Specimen01-03

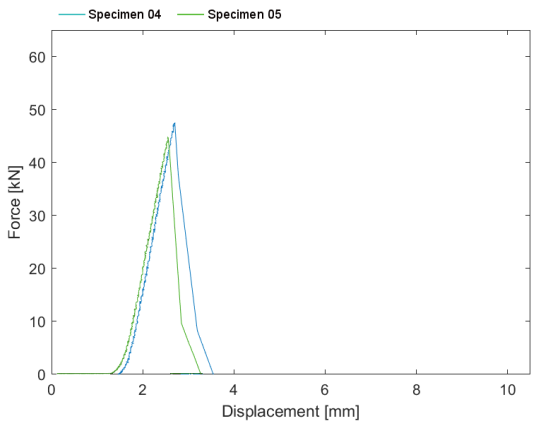

(b) CCI+DW20_4-6_1 Specimen04-05

Figure 31: CCI+DW20_4-6_1: cylinder force vs displacement

To determine the transition to the ductile failure, the experimental speeds of the following CCI test series are reduced gradually.

CCI+DW20_0,23

Unsieved commercial crushed ice, mixed with distilled water of ambient temp. and loaded with a ***test speed of 0,23 mm/s*** *($\dot{\epsilon} = 1,31 \cdot 10^{-3}$)*

Table 5 represents the results of the CCI+DW20_0,23 test series.

Table 5: CCI+DW20_0,23

Specimen No.	Temp [°C]	Force_Cyl [kN]	Pressure_Cyl [MPa]	Failure Mode
1	-5,27	30,57	3,92	brittle
2	-9,26	45,55	5,85	brittle
3	-9,21	43,25	5,55	brittle
4	-9,18	42,19	5,42	brittle
5	-9,38	42,67	5,48	brittle
Mean Value	-8,46	40,85	5,24	
Standard Deviation			0,76	
COV			0,14	

As Figure 32 shows, brittle failure is also recognizable for this experimental speed. The standard deviation here is 0,76. Noteworthy is the inequality of temperatures prevailing during the tests which doesn't mean that the ambient temperature in the container matches the temperature of the core of the samples.

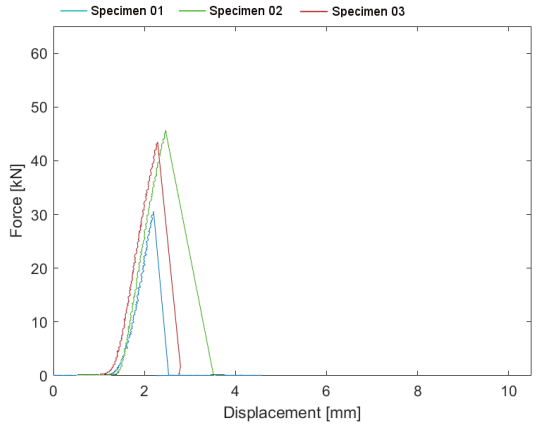

(a) CCI+DW20_0,23 Specimen01-03

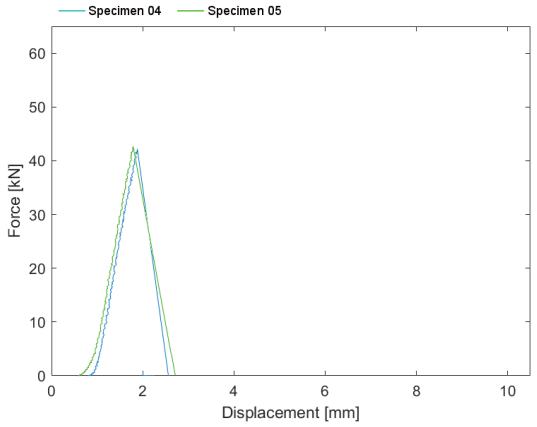

(b) CCI+DW20_0,23 Specimen04-05

Figure 32: CCI+DW20_0,23: cylinder force vs displacement

CCI+DW20_0,165

Unsieved commercial crushed ice, mixed with distilled water of ambient temp. and loaded with a ***test speed of 0,165 mm/s*** *($\dot{\epsilon} = 9,43 \cdot 10^{-4}$)*

Since this tests series is only served to detect the transition area and the first two samples continued to show brittle failure with an additional high deviation, no further tests are carried out. This is why a statistical statement is limited here. Nevertheless, the resulting values are listed together with the measurements in Table 6.

Table 6: CCI+DW20_0,165

Specimen No.	Temp [°C]	Force_Cyl [kN]	Pressure_Cyl [MPa]	Failure Mode
1	-8,26	53,75	6,90	brittle
2	-8,86	38,40	4,93	brittle
Mean Value	-8,56	46,08	5,91	
Standard Deviation			1,39	
COV			0,24	

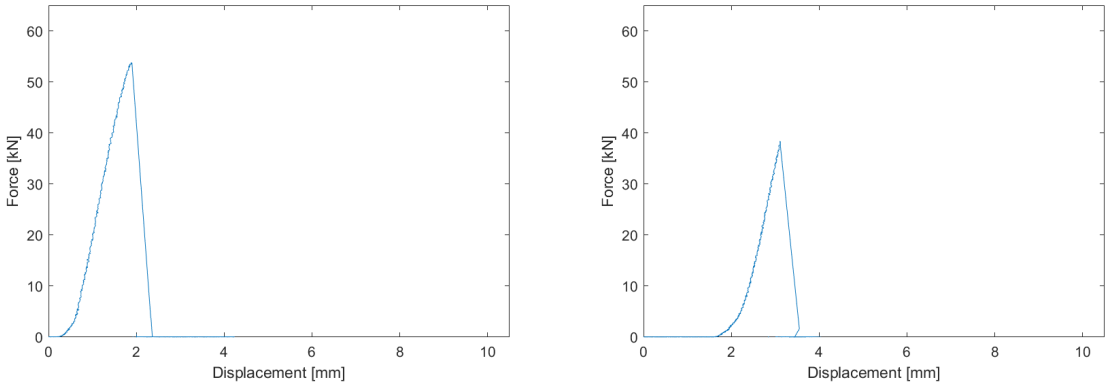

(a) CCI+DW20_0,165 Specimen01 (b) CCI+DW20_0,165 Specimen02

Figure 33: CCI+DW20_0,165: cylinder force vs displacement

CCI+DW20_0,13

Unsieved commercial crushed ice, mixed with distilled water of ambient temp. and loaded with a ***test speed of 0,13 mm/s*** *($\dot{\epsilon} = 7,43 \cdot 10^{-4}$)*

At a test speed of 0,13 mm/s, the course of the curves change. As seen in Figure 34, after reaching the peak, there is not a direct drop in force, but a short range in which the force decreases before brittle-like failure. However, the samples also have a high dispersion with a standard deviation of 1,90 like represented in Table 7.

Table 7: CCI+DW20_0,13

Specimen No.	Temp [°C]	Force_Cyl [kN]	Pressure_Cyl [MPa]	Failure Mode
1	-8,37	49,07	6,30	rather brittle
2	-8,07	47,61	6,11	rather brittle
3	-8,01	22,75	2,92	rather brittle
Mean Value	-8,15	39,81	5,11	
Standard Deviation			1,90	
COV			0,37	

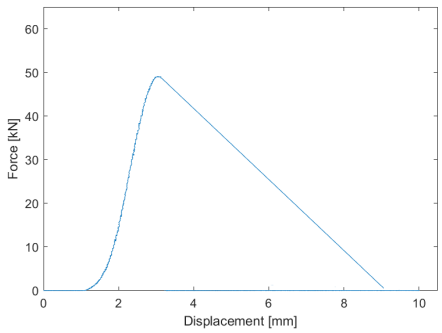

(a) CCI+DW20_0,13 Specimen01

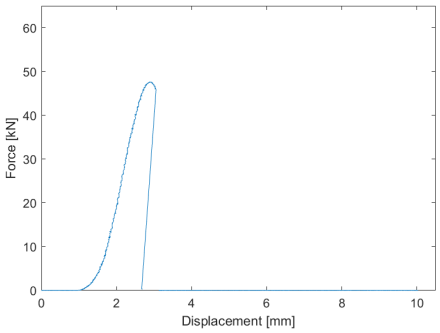

(b) CCI+DW20_0,13 Specimen02

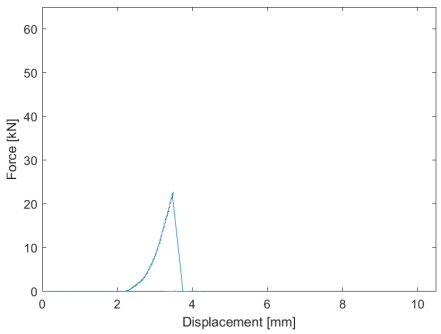

(c) CCI+DW20_0,13 Specimen03

Figure 34: CCI+DW20_0,13: cylinder force vs displacement

CCI+DW20_0,12

Unsieved commercial crushed ice, mixed with distilled water of ambient temp. and loaded with a ***test speed of 0,12 mm/s*** *($\dot{\epsilon} = 6,86 \cdot 10^{-4}$)*

This test series shows similar failure patterns as in the earlier series but with a way lower standard deviation of about 0,22 like shown in Table 8.

Table 8: CCI+DW20_0,12

Specimen No.	Temp [°C]	Force_Cyl [kN]	Pressure_Cyl $[MPa]$	Failure Mode
1	-9,13	48,44	6,22	rather brittle
2	-9,27	51,63	6,63	rather brittle
3	-9,13	49,01	6,29	rather brittle
Mean Value	-9,18	49,69	6,38	
Standard Deviation			0,22	
COV			0,03	

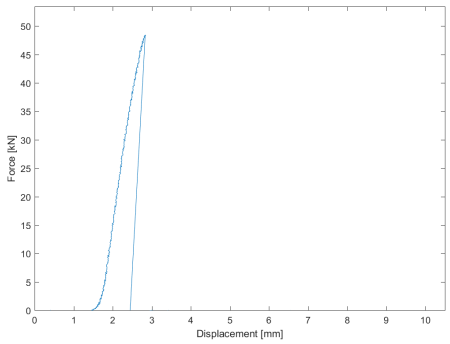

(a) CCI+DW20_0,12 Specimen01

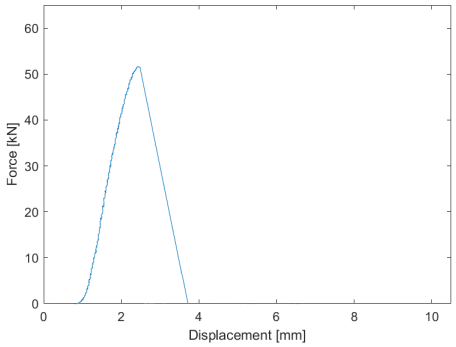

(b) CCI+DW20_0,12 Specimen02

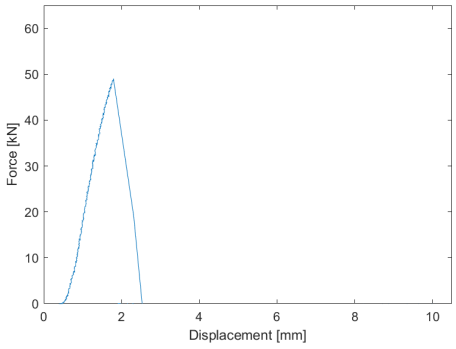

(c) CCI+DW20_0,12 Specimen03

Figure 35: CCI+DW20_0,12: cylinder force vs displacement

CCI+DW20_0,11

Unsieved commercial crushed ice, mixed with distilled water of ambient temp. and loaded with a ***test speed of 0,11 mm/s*** *($\dot{\epsilon} = 6,29 \cdot 10^{-4}$)*

The present test series shows both ductile and brittle failure modes as presented in Figure 36. This is identified as an indicator of the transition range. Although a statistical evaluation of three samples is difficult, it can be seen that the measured cylinder forces differ only slightly with a standard deviation of 0,14

Table 9: CCI+DW20_0,11

Specimen No.	Temp [°C]	Force_Cyl [kN]	Pressure_Cyl [MPa]	Failure Mode
1	-8,70	48,60	6,24	ductile
2	-8,94	49,16	6,31	rather ductil
3	-8,72	50,65	6,50	rather brittle
Mean Value	-8,79	49,47	6,35	
Standard Deviation			0,14	
COV			0,02	

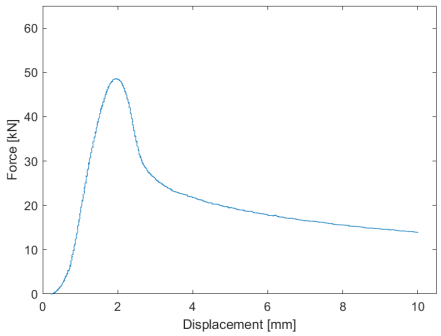

(a) CCI+DW20_0,11 Specimen01

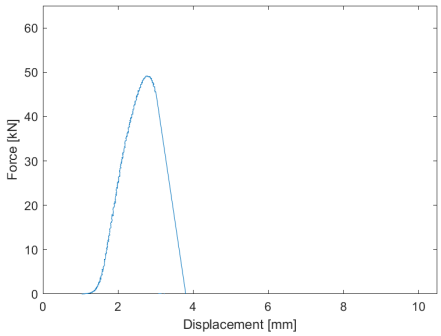

(b) CCI+DW20_0,11 Specimen02

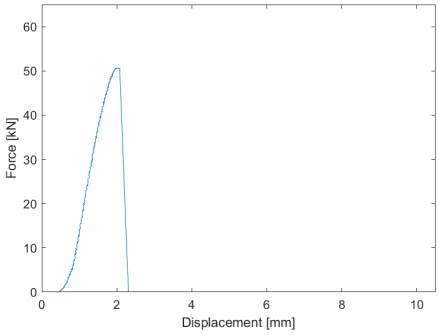

(c) CCI+DW20_0,11 Specimen03

Figure 36: CCI+DW20_0,11: cylinder force vs displacement

CCI+DW20_0,1

Unsieved commercial crushed ice, mixed with distilled water of ambient temp. and loaded with a ***test speed of 0,1 mm/s*** *($\dot{\epsilon} = 5,71 \cdot 10^{-4}$)*

From a test speed of 0,1 mm/s, purely ductile failure courses occur for all specimen within this test series. Due to these observations the transition from ductile to brittle behavior is in a very small range. This isn't coincide with other researches, that state a wide range like seen in chapter 3.

Table 10: CCI+DW20_0,1

Specimen No.	Temp [°C]	Force_Cyl [kN]	Pressure_Cyl [MPa]	Failure Mode
1	-9,48	60,57	7,77	ductile
2	-9,13	56,41	7,24	ductile
3	-6,49	56,19	7,21	ductile
4	-8,10	53,71	6,89	ductile
5	-7,62	56,49	7,25	ductile
6	-7,47	59,16	7,59	ductile
7	-6,37	58,23	7,47	ductile
8	-7,65	55,93	7,18	ductile
9	-7,57	57,15	7,34	ductile
Mean Value	-7,76	57,09	7,33	
Standard Deviation			0,26	
COV			0,04	

This phenomenon can be reflected again in the following plots of Figure 37 which are typical for ductile behavior. There is no abrupt fracture after reaching the peak force but a further deformation with a steady decrease of the force until the termination after the hydraulic cylinder reaches a displacement of 10 mm.

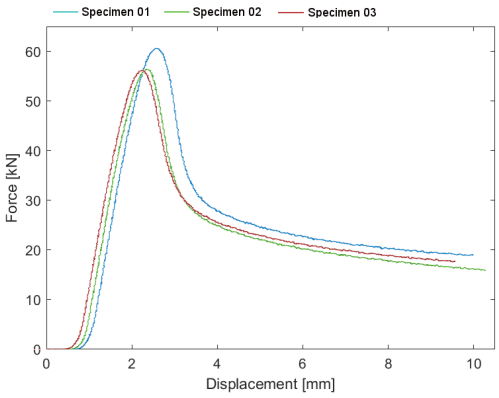

(a) CCI+DW20_0,1 Specimen01-03

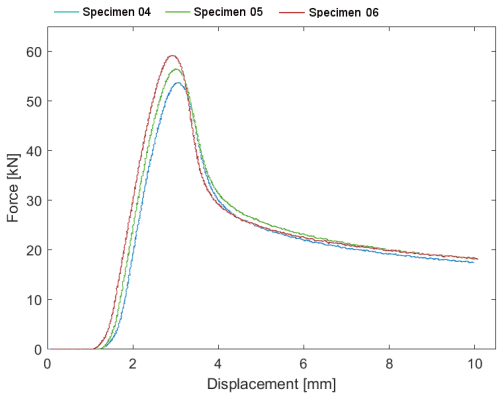

(b) CCI+DW20_0,1 Specimen04-06

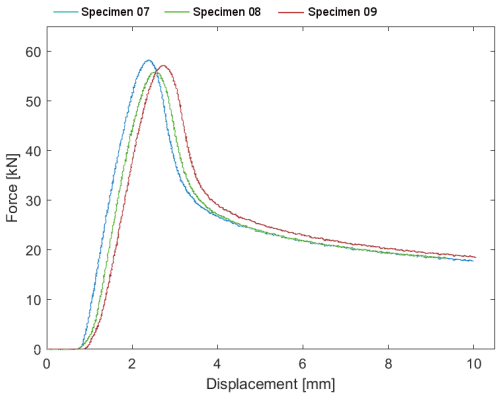

(c) CCI+DW20_0,1 Specimen07-09

Figure 37: CCI+DW20_0,1: cylinder force vs displacement

5.2 Self-Made Crushed Ice

After analyzing the commercial crushed ice samples, the next thing to follow will be the self-made crushed ice test series. These include two differently sieved samples series which are both loaded at a test speed of one millimeter per second.

SMCI+DW20_6-11_1

Self-made crushed ice with 6 to 11 mm fragments, mixed with distilled water of ambient temp. and loaded with a ***test speed of 1 mm/s*** *($\dot{\epsilon} = 5,71 \cdot 10^{-3}$)*

At this test speed, brittle failure forms are evident again, just like in the case of the CCI test series. The measured data can be found in Table 11.

Table 11: SMCI+DW20_6-11_1

Specimen No.	Temp [°C]	Force_Cyl [kN]	Pressure_Cyl [MPa]	Failure Mode
1	xx	43,32	5,56	brittle
2	xx	23,59	3,03	brittle
3	xx	41,63	5,34	brittle
4	xx	22,94	2,94	brittle
5	xx	31,41	4,03	brittle
6	xx	38,08	4,89	brittle
7	xx	35,89	4,61	brittle
8	xx	39,35	5,05	brittle
Mean Value	xx	34,53	4,43	
Standard Deviation			1,00	
COV			0,23	

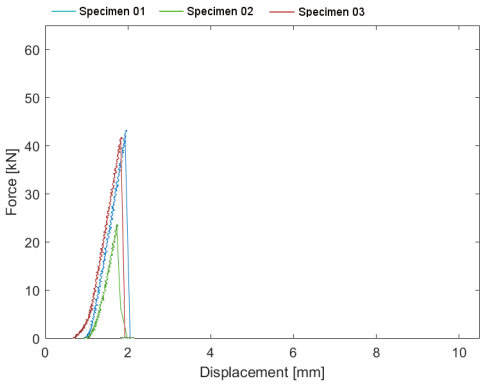

(a) SMCI+DW20_6-11_1 Specimen01-03

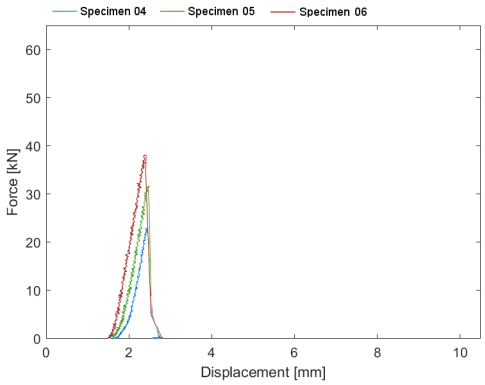

(b) SMCI+DW20_6-11_1 Specimen04-06

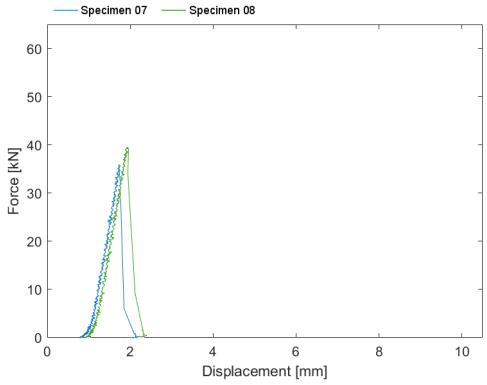

(c) SMCI+DW20_6-11_1 Specimen07-08

Figure 38: SMCI+DW20_6-11_1: cylinder force vs displacement

SMCI+DW20_4-6_1

Self-made crushed ice with 4 to 6 mm fragments, mixed with distilled water of ambient temp. and loaded with a ***test speed of 1 mm/s*** *($\dot{\epsilon} = 5,71 \cdot 10^{-3}$)*

The samples of this test series consist of smaller ice fragments compared to the previous one as they are sieved with finer mesh sizes of 4 and 6 mm. This has a positive effect and is reflected in a lower standard deviation which is only 0,37 here.

Table 12: SMCI+DW20_4-6_1

Specimen No.	Temp [°C]	Force_Cyl [kN]	Pressure_Cyl $[MPa]$	Failure Mode
1	-8,24	33,76	4,33	brittle
2	-7,83	38,02	4,88	brittle
3	-8,09	39,25	5,04	brittle
Mean Value	-8,05	37,01	4,75	
Standard Deviation			0,37	
COV			0,08	

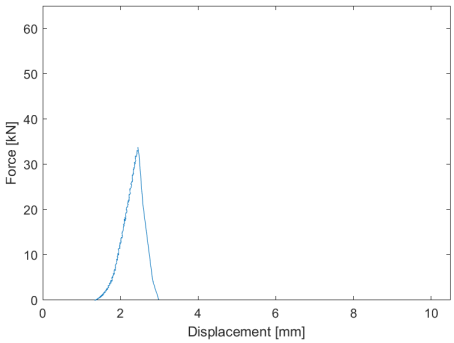

(a) SMCI+DW20_4-6_1 Specimen01

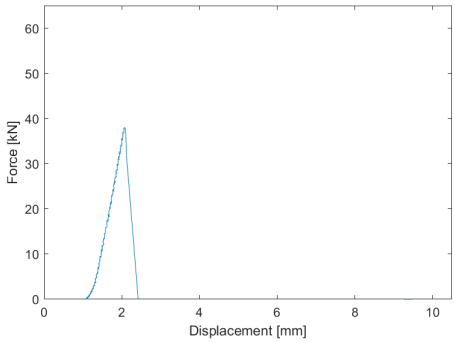

(b) SMCI+DW20_4-6_1 Specimen02

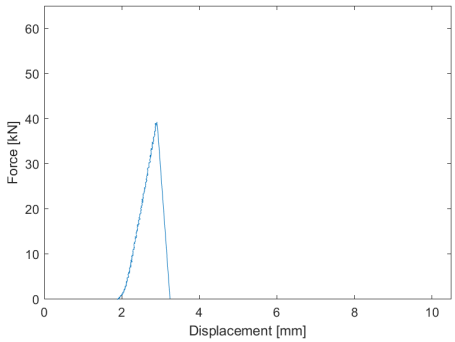

(c) SMCI+DW20_4-6_1 Specimen03

Figure 39: SMCI+DW20_4-6_1: cylinder force vs displacement

5.3 Deep Freezer Columnar Ice

For comparison to previous researches of the institute and in order to get a reference, also a series from the deep freezer is tested. Here, the samples are not made with crushed ice particles but pure distilled water that can only freeze in one direction, resulting in columnar grown ice.

DF_DW20_1

Columnar ice generated in the deep freezer with pure distilled water of ambient temp. and loaded with a ***test speed of 1 mm/s*** *($\dot{\epsilon} = 5,71 \cdot 10^{-3}$)*

As already observed in previous research projects, the DF samples show a high variance despite the newly installed experimental set-up. The measured data can be found in Table 13.

Table 13: DF_DW20_1

Specimen No.	Temp [°C]	Force_Cyl [kN]	Pressure_Cyl $[MPa]$	Failure Mode
1	-5,88	48,93	6,28	brittle
2	-7,63	52,29	6,71	brittle
3	-7,74	51,45	6,60	brittle
4	-7,74	37,36	4,80	brittle
5	-7,56	54,61	7,01	brittle
6	-6,88	39,49	5,07	brittle
7	-7,55	47,50	6,10	brittle
8	-8,02	35,16	4,51	brittle
9	-7,18	50,32	6,46	brittle
Mean Value	-7,35	46,35	5,95	
Standard Deviation			0,91	
COV			0,15	

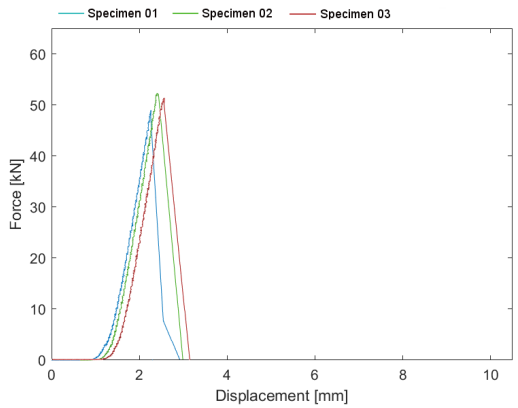

(a) DF_DW20_1 Specimen01-03

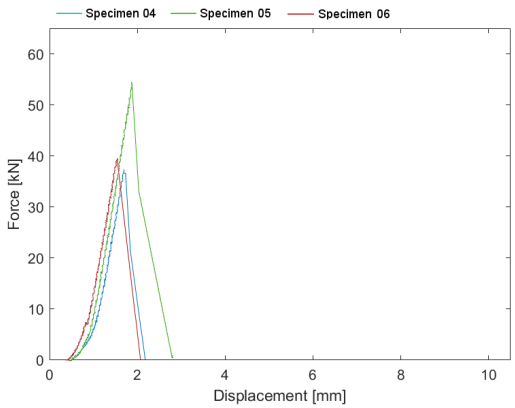

(b) DF_DW20_1 Specimen04-06

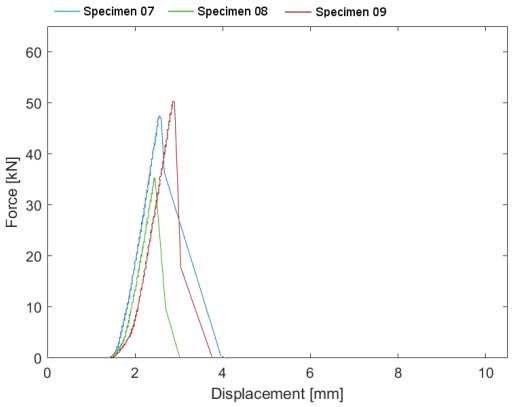

(c) DF_DW20_1 Specimen07-09

Figure 40: DF_DW20_1: cylinder force vs displacement

6 Comparison and Discussion

The previous chapter included a tabular summary of the strength characteristics that are determined metrologically from the individual experiments, as well as the related graphical display of the cylinder force over its displacement. Using the simplified statistical view of these results, the three different production methods can be compared at this point.

For an overview of all measured maximum forces of each test series, the following Table 14 is given first. As already mentioned, the low number of specimen of some test series is striking here, which impedes a statistical statement. Further informations, described in the previous chapters are summarized in Table 15.

Table 14: Overview of the cylinder forces in kN of all test series

	Specimen No.								
Test Series	1	2	3	4	5	6	7	8	9
SMCI+DW20_6-11_1	43,32	23,59	41,63	22,94	31,41	38,08	35,89	39,35	xx
SMCI+DW20_4-6_1	33,76	38,02	39,25	xx	xx	xx	xx	xx	xx
CCI+DW20_1	45,55	48,01	52,44	52,27	49,33	50,32	46,56	xx	xx
CCI+DW20_4-6_1	52,18	50,86	44,66	47,49	44,66	xx	xx	xx	xx
CCI+DW20_0,23	30,57	45,55	43,25	42,19	42,67	xx	xx	xx	xx
CCI+DW20_0,165	53,75	38,40	xx	xx	xx	xx	xx	xx	xx
CCI+DW20_0,13	49,07	47,61	22,75	xx	xx	xx	xx	xx	xx
CCI+DW20_0,12	48,44	51,63	49,01	xx	xx	xx	xx	xx	xx
CCI+DW20_0,11	48,60	49,16	50,65	xx	xx	xx	xx	xx	xx
CCI+DW20_0,1	60,57	56,41	56,19	53,71	56,49	59,16	58,23	55,93	57,15
DF_DW20_1	48,93	52,29	51,45	37,36	54,61	39,49	47,50	35,16	50,32

Table 15: Summarizing table

Test series	Grain size [mm]	Strain rate [s^{-1}]	Min F_{Cyl} [kN]	Max F_{Cyl} [kN]	Mean F_{Cyl} [kN]	Min stress [MPa]	Max stress [MPa]	Mean stress [MPa]	Standard deviation [-]	Failure mode
SMCI+DW20_6-11_1	6,06	$5,71 \cdot 10^{-3}$	22,94	43,32	34,53	2,94	5,56	4,43	1,00	brittle behavior with conical fracture
SMCI+DW20_4-6_1	4,12	$5,71 \cdot 10^{-3}$	33,76	39,25	37,01	4,33	5,04	4,75	0,37	brittle behavior with conical fracture
CCI+DW20_1	1,68	$5,71 \cdot 10^{-3}$	45,55	52,44	49,21	5,85	6,73	6,32	0,34	brittle behavior with conical fracture
CCI+DW20_4-6_1	1,49	$5,71 \cdot 10^{-3}$	44,66	52,18	47,97	5,73	6,70	6,16	0,45	brittle behavior with conical fracture
CCI+DW20_0,23	1,68	$1,31 \cdot 10^{-3}$	30,57	45,55	40,85	3,92	5,85	5,24	0,76	brittle behavior with conical fracture
CCI+DW20_0,165	1,68	$9,43 \cdot 10^{-4}$	38,40	53,75	46,08	4,93	6,90	5,91	1,39	brittle behavior with conical fracture
CCI+DW20_0,13	1,68	$7,43 \cdot 10^{-4}$	22,75	49,07	39,81	2,92	6,30	5,11	1,90	brittle behavior with conical fracture
CCI+DW20_0,12	1,68	$6,86 \cdot 10^{-4}$	48,44	51,63	49,69	6,22	6,63	6,38	0,22	brittle-like behavior with conical fracture
CCI+DW20_0,11	1,68	$6,29 \cdot 10^{-4}$	48,60	50,65	49,47	6,24	6,50	6,35	0,14	brittle and ductile behavior with conical fracture and plastic bulging
CCI+DW20_0,1	1,68	$5,71 \cdot 10^{-4}$	53,71	60,57	57,09	6,89	7,77	7,33	0,26	ductile behavior with plastic bulging
DF_DW20_1	10,12	$5,71 \cdot 10^{-3}$	35,16	54,61	46,35	4,51	7,01	5,95	0,91	brittle behavior with axial fracture

For a first comparison of the production methods, Figure 41 visualizes the mean values of the cylinder force for each test series. Since the compressive strength of ice depends on the strain rate, we look at the series of tests performed at a uniform experimental speed of 1 mm/s. The minimum and maximum cylinder forces can be considered as fault indicators.

Initially we have a closer look at the specimens of pure distilled water which are generated in the deep freezer at -60 °C and are solidificated in columnar shape. Compared to the other test series at 1 mm/s, the DF_DW20 test series has the highest maximum force and a comparable mean value, but with a standard deviation of 0,91 also a high variance of measured peak forces. This scattering has also noted in some pilot tests of previous researches. One explanation can be found in the internal texture which is distinguishable from the thin sections in Figure 21. The grain structure varies significantly depending on the growth of the columns determined by the geometric selection. This results in different strength values depending on the orientation of the columns to the introduced direction of force. The fracture pattern also shows significant differences as the sizes of the shards formed through axial splitting are completely different to the ones resulting in the case of conical fracture. All in all this manufacturing process admittedly models natural ice formations like common in the polar ice sheet the closest but does not enable reproducible laboratory specimen due to strongly different growth textures.

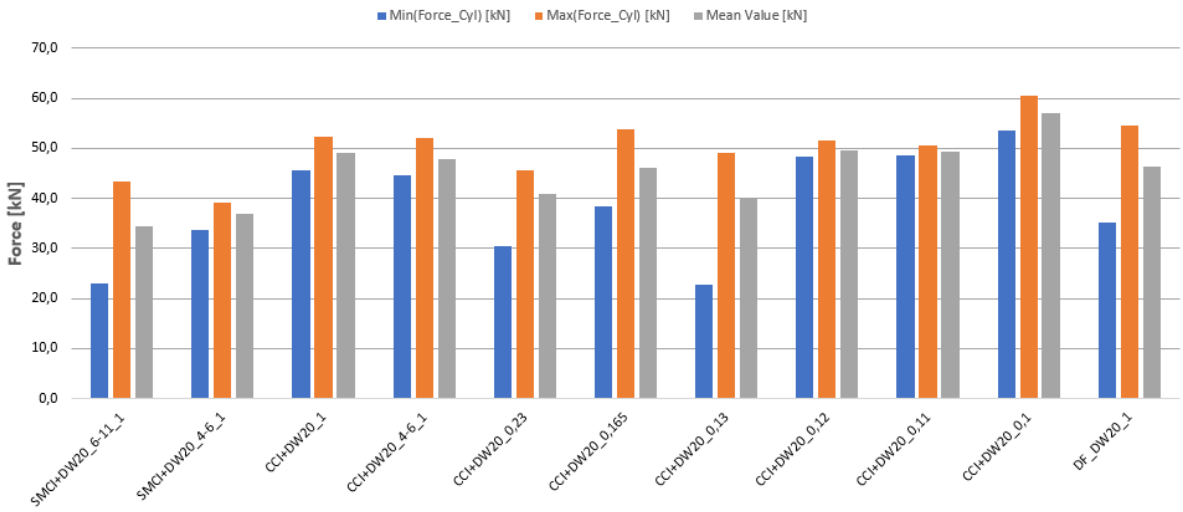

Figure 41: Comparison of the peak cylinder forces and the mean value

Ensuing from the desire for reproducible samples and to improve the scattering of the results by controlling the inner structure, crushed ice is used. In the case of self-made crushed ice Figure 41 shows that these two test series have the lowest strength values with a mean force of 34,53 kN (SMCI+DW20_6-11_1) and 37,01 kN (SMCI+DW20_4-6_1). In addition the samples sieved with a mesh size of 6 and 11 mm are highly scattered

with a standard deviation of 1,0. The specimen with the smaller crushed ice fragments (4-6 mm) do not have the same dispersion. But it has to be noted that this series only includes three specimen.

In comparison, the commercial crushed ice samples performed at the same test speed of 1 mm/s show significantly higher mean strength values and a lower measure of dispersion. These differences are due to the grain structure. When looking at the self-made crushed ice thin sections from Figure 17 again a clearly defined and uniform grain structure with only a very small amount of air inclusions can be seen. The commercial crushed ice thin sections in Figure 20 show a higher amount of air pockets. In addition the crushed ice pieces are made from tap water rather than from pure distilled water. But these facts are not to be disadvantages in terms of strength. The difference is in the much finer grain size of the commercial crushed ice pieces. This influence is already described by Schulson and Duval (2009) [30]. Figure 42 shows their observations and represents the unconfined brittle compressive strength of fresh water granular ice over the grain size d.

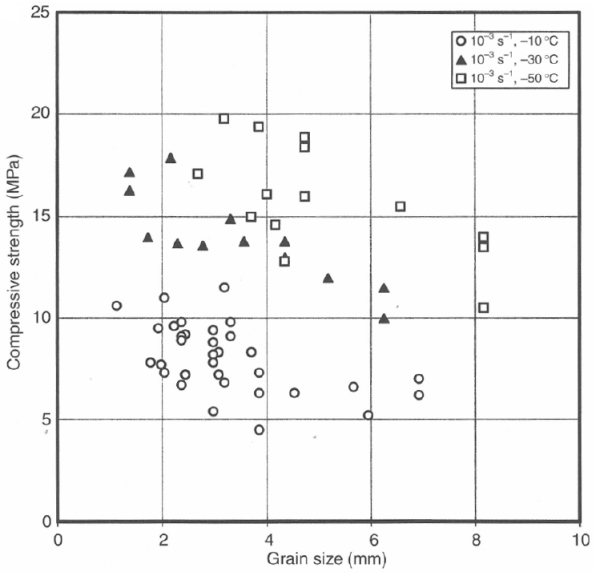

Figure 42: Unconfined brittle compressive strength of granular fresh water ice over grain size [30]

Although the results in this figure are scattered, it can be seen that the compressive strength decreases with increasing grain size even though to a minor degree. An explanation for that is based on researches of ceramics and suggests that there could be a higher density of crack-tip deformation damage with decreasing grain size [30]. By combining the data from Table 15, the following Figure 43 is shown that outlines the same trend for the three manufacturing methods and its extensions. Only the DF samples do not follow this observations cause they are columnar structured which is not directly comparable with the granular test series.

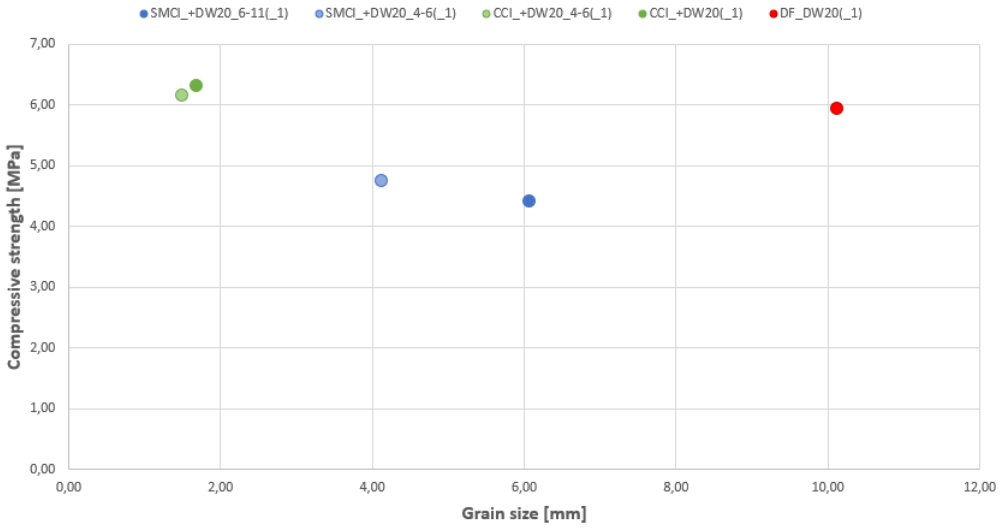

Figure 43: Compressive strength at a test speed of 1 mm/s vs grain size

However, Figure 42 additional shows the influence of the temperature on the compressive strength. At a constant axial strain rate, the compressive strength of the ice decreases with increasing temperature. This is rooted in the fact that viscous behavior and recovery effects such as dislocation climb and dislocation annihilation increase at higher temperatures [32]. Since the prevailing temperature during the experiments carried out here was not constant, this could also have led to differences in the compressive strength. Anyway it has to be noted that the prevailing temperature in the container is not the same as the temperature of the core of the samples which is not measured during the tests. Nonetheless, it is clear that the samples of the commercial crushed ice series are in the ascendancy over the deep freezer and self-made crushed ice samples with regard to the compressive strength and the dispersion within one series. So the next section uses this manufacturing method to show the speed dependence of compressive strength and failure modes.

Different combinations of compressive stress states and strain rates result in changes of behavior of ice. By varying the strain rate of the commercial crushed ice test series, the range of brittle and ductile behavior as well as the transitional area between them can be identified. For this Figure 44 shows the mean stress over the strain rate for each test series. The three production methods are differentiated in color again. The vertical bars can be understood as fault indicators and only show the minimum and maximum measured force and are therefore asymmetrical.

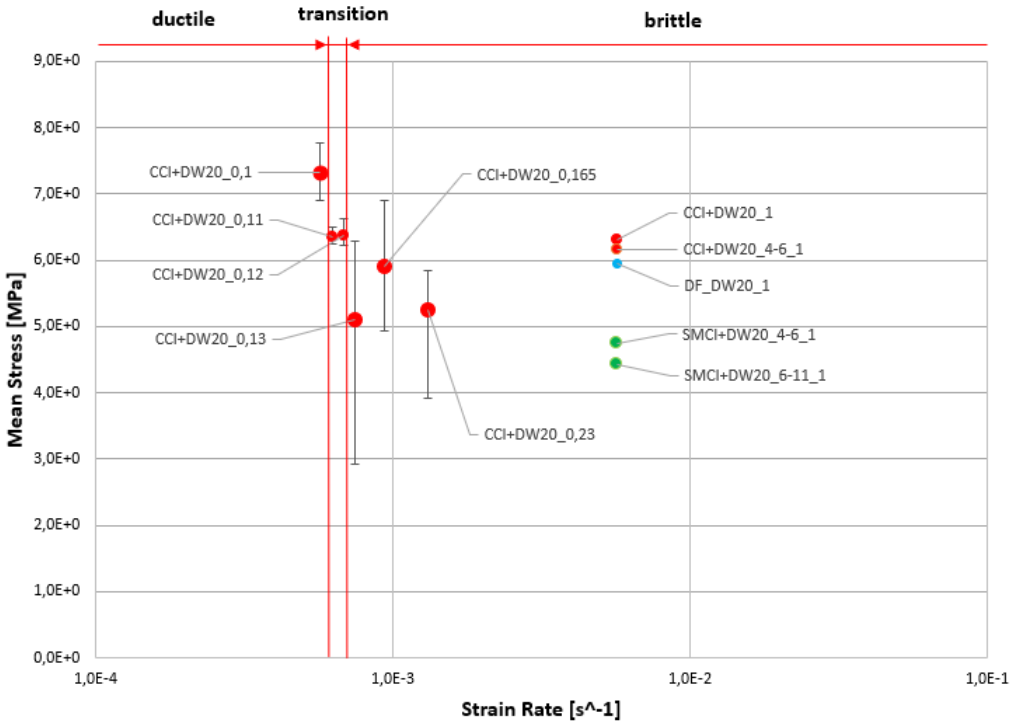

Figure 44: Mean stress vs strain rate

It can be seen, that the highest strength values are achieved at the lowest strain rate. Especially CCI+DW20_0,1 and the CCI+DW20_0,11 as well as the CCI+DW20_0,12 are standing out here. It is striking that these test series also have the lowest scattering. CCI+DW20_0,11 and CCI+DW20_0,12 are found to be in the transition range, where both ductile and brittle failure processes occur within one test series. Thereof the transition area can be defined in a small strain rate spectrum of about $6,86 \cdot 10^{-4}$ to $6,29 \cdot 10^{-4}$. This spectrum admittedly matches within the transition range observed in experiments of Schulson (1999) [29], but does not have the same width like seen again in Figure 7. Yue et al. (2009) [38] defines an even larger transitional range that would include all of the results measured here. These differences can not be clarified in this context. Nevertheless the high strength values in this range are consistent with previous observations as described in Chapter 3.4. One possible reason for the differences could reside in the manufacturing process and the composition of the laboratory test specimens. These informations are not known for some of the conducted experiments of other researches.

In order to be able to classify and validate the results achieved here, they are compared and summarized with those from a database [19]. This database includes ice data from various research works. By selecting certain criteria, the data can be adapted to your own experiments. In addition to the own values, Figure 45 shows the database entries from Schulson, E. (1990) [28], Mellor, M. and Cole, D. (1982) [22] and Haynes, F. and Mellor, M. (1977) [11] for uniaxial compression tests of polycrystalline and granular ice,

made of distilled water or deionized distilled water. These tests are conducted at a temperature between -5 and -15 °C.

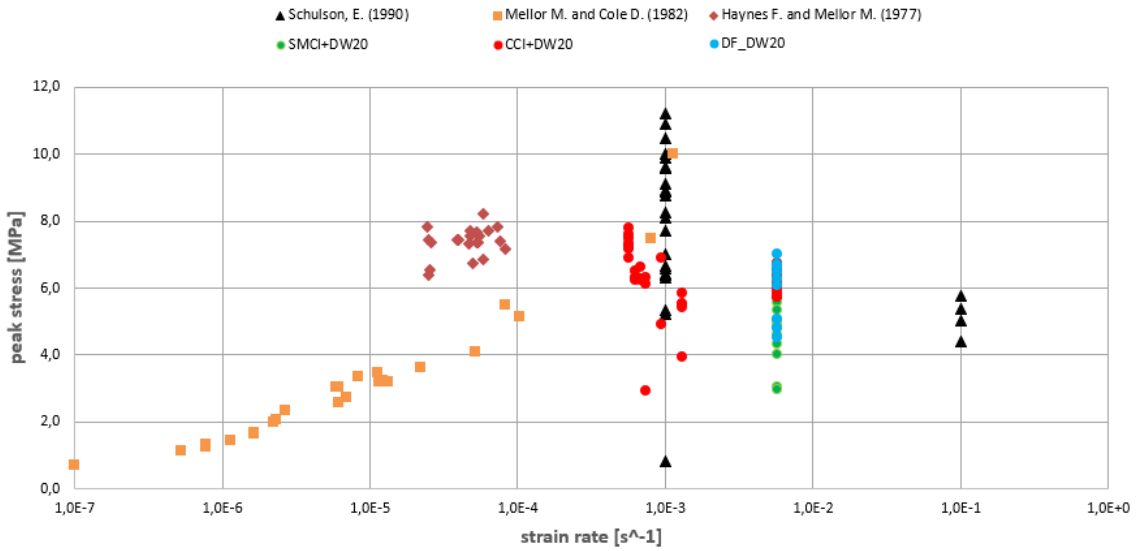

Figure 45: Peak stress vs strain rate for polycrystalline and granular ice [19], extended with own values

The several research works can be identified by the various marking forms and colors. In addition, the values obtained here are color coded depending on the production method. The resulting data from Haynes, F. and Mellor, M. (1977) and Mellor, M. and Cole, D. (1982) both show sheer ductile material behavior while the data from Schulson, E. (1990) indicates brittle behavior. The transition area is not specified in the database. But it can be seen that the progression of the graph approximately reflects slightly the results of Schulson's earlier research, as seen in Figure 7. At that point the highest strength values are reflected in the transition range. All in all the values achieved in this thesis, follow this course and are comparable with those from previous researches.

Naturally, ships encounter sea ice when sailing into polar regions. The ice out of saltwater differs significantly from the laboratory freshwater ice in many ways. Especially the composition of the dissolved salts plays a decisive role. As an outlook, some sea ice data are presented in Figure 46 as a collection of the database [19] in comparison with the results of the laboratory tests achieved here.

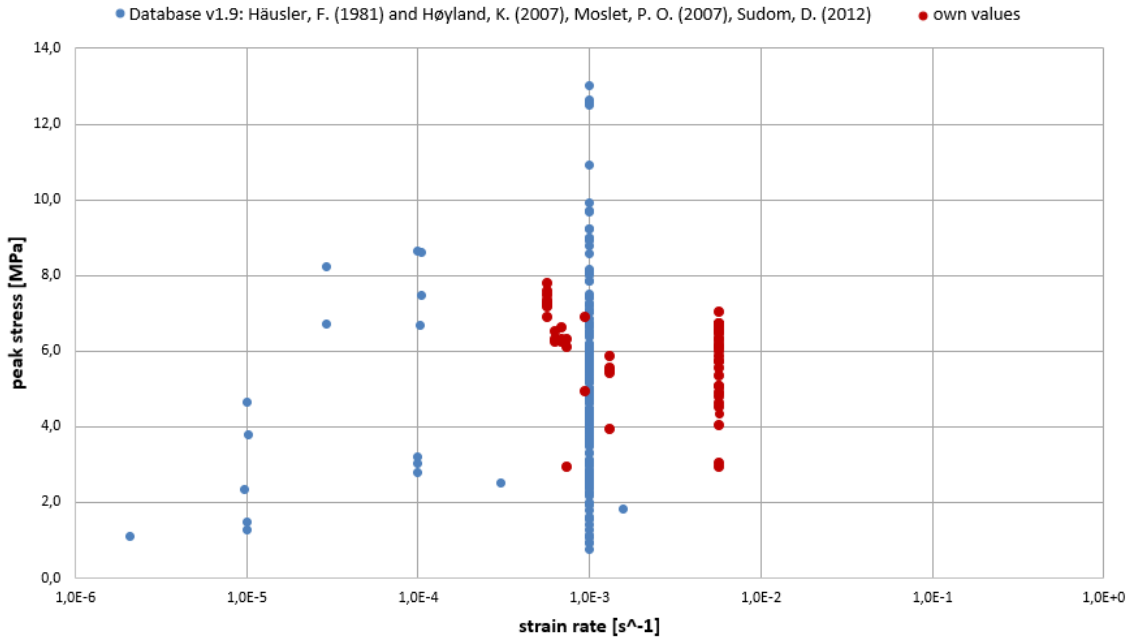

Figure 46: Peak stress vs strain rate for sea ice [19], extended with own values

The blue marked data points in the figure are originally from Häusler F. (1981) [10] and Hoyland K. (2007) [14] together with Moslet, P. O. (2007) [24] and Sudom, D. (2012) [34]. They performed uniaxial compression tests of columnar grown sea water ice, loaded along the columns at a temperature between -5 and -15 °C. The red data points define all the results of the compression tests, investigated in the scope of this thesis. Since the points of the sea ice tests scatter strongly, the strength values obtained by using the three laboratory manufacturing methods can be found in the same range. To sum up this shows that these results represent a good first approximation to that of sea ice.

7 Summary

To sum up, the three production methods of laboratory-made freshwater ice could be compared in simple compression tests relating to the strength values on the basis of the ice properties and a uniform experimental speed. It can be stated that the results of the investigated tests are differ significantly. The columnar grown samples from the deep freezer (DF_DW20_1) have scattering strength values due to its various grain structure conditioned by the geometric selection and growth propagation of the grains. Therefore it can not provide new insights despite the new test set-up. In the case of self-made crushed ice test series a homogeneous and undisturbed grain structure could be achieved but the larger grain size effected lower strength values with a high dispersion. In terms of strength, the method using commercial crushed ice mixed with distilled water has achieved the best results. This is mainly effected due to the finer grain structure which leads to a higher density of crack-tip deformation damage. Nevertheless, some commercial crushed ice test series also have a high degree of scattering, so that this production

method also does not yield any satisfactory results in terms of reproducibility.

Based on the commercial crushed ice test series, it has been possible to observe the speed dependence of the compression strength and the different failure modes by varying the strain rate. Beneath a strain rate of $5,71 \cdot 10^{-4}$ ductile behavior could be observed. In a small spectrum between the strain rates of $6,29 \cdot 10^{-4}$ and $6,86 \cdot 10^{-4}$ the transition range could be identified. All series of tests above this strain rate have shown sheer brittle behavior. It is noticeable that the degree of scattering gets lower with decreasing experimental speed. But due to possible differences in the manufacturing process, varying internal structures and temperature inequality no further correlation could be established between the failure modes and the achieved compression strength so that the results of previous research can not be compared or confirmed. With regard to sea ice, however, it can be said that the results obtained here provide a good first approximation but leave latitude for further researches.

8 Suggestion for Further Work

The present work dealt with the first ice compression tests on a newly installed setup. For further work with the same focus of research, it shows some possibilities for improvement. On the one hand, for a better statistical evaluation, an appropriate number of samples should be used for each test series. On the other hand, in the previous chapter the temperature influence on the strength was shown, which was neglected during these experiments most widely. These two points offer potential for an improved comparison of the results.

In addition, the self-made crushed ice samples could be further processed. By reducing the mesh size of the sieving process, the ice pieces could be reduced by size to refine the granular grain structure. In doing so, the theory that a higher compressive strength is produced by smaller grains, could be followed as well as the weakening influence of air inclusions we found in the commercial crushed ice pieces.

Furthermore, it could still be attempted to achieve the granular ice structure in other ways. For instance by the means of snow slush or small ice crystals that are introduced on the surface at the beginning of the freezing process from which the further structure can form.

If applicable results reveal here, the experiments have to be extended to salt water grown ice to get closer to the natural conditions, ships and offshore structures face to.

References

[1] Cmglee. Phase diagram of water, 2015. URL `https://commons.wikimedia.org/wiki/File:Phase_diagram_of_water.svg`.

[2] David M. Cole. Preparation of polycrystalline ice specimens for laboratory experiments. *Cold Regions Science and Technology*, 1(2):153–159, 1979. ISSN 0165232X. doi: 10.1016/0165-232X(79)90007-7.

[3] Claude Daley. Sea ice engineering: theory and application. 2010.

[4] Duval P., M. F. Ashby, and Anderman I. Rate-controlling processes in the creep of polycrystalline ice. 1982.

[5] E04 Committee. Test methods for determining average grain size, 2012.

[6] Victor Flatt. *Influencing Factors of Ice-Structure-Interaction Experiments*. Bachelor thesis, Technical University of Hamburg-Harburg, Hamburg, 15.10.2015.

[7] R. Frederking. Plane-strain compressive strength of columnar-grained and granular-snow ice. *Journal of Glaciology*, 18(80):505–516, 1977. ISSN 0022-1430. doi: 10.1017/S002214300002116X.

[8] Gold L. W. Process of failure in ice. *Research Paper*, (450), 1970.

[9] Narayana Golding. Compressive shear faulting in ice loaded triaxially: The influence of confinement. 2011.

[10] Häusler F. Dreidimensionales bruchkriterium für meer-eis: Unpublished.

[11] F. D. Haynes and M. Mellor. Measuring the uniaxial compressive strength of ice. *Journal of Glaciology*, 1977(81):213–223.

[12] Peter Victor Hobbs. *Ice physics*. Oxford classic texts in the physical sciences. Oxford Univ. Press, Oxford, 2010. ISBN 9780199587711.

[13] Roger LeB Hooke. *Principles of glacier mechanics*. Cambridge University Press, Cambridge, second edition edition, 2005. ISBN 0521544165. doi: 10.1017/CBO9780511614231.

[14] Knut V. Høyland. Morphology and small-scale strength of ridges in the northwestern barents sea. *Cold Regions Science and Technology*, 48(3):169–187, 2007. ISSN 0165232X. doi: 10.1016/j.coldregions.2007.01.006.

[15] Malte Humpert and Andreas Raspotnik. The future of arctic shipping, 2012. URL `http://www.thearcticinstitute.org/the-future-of-arctic-shipping/`.

[16] Jacka, Tim H, Jun, and Li. Flow rates and crystal orientation fabrics in compression of polycrystalline ice at low temperatures and stresses. *Physics of ice core records*, pages 83–102, 2000.

[17] Jones Stephen J. and H. A. M. Chew. Effect of sample and grain size on the compressive strength of ice. *Annals of Glaciology*, 1983(4).

[18] Ian J. Jordaan. Mechanics of ice-structure interaction. *Engineering Fracture Mechanics*, 2001(68), 1999.

[19] Leon Kellner. Establishing a common data base of ice experiments and using machine learning to understand and predict ice behavior. 2018.

[20] Kleitz Ina. *Physikalische Eigenschaften und Spurenstoffe im groenlaendischen Eis*. PhD thesis, Ernst-Moritz-Arndt Universität Greifswald, Greifswald, 12.07.2013.

[21] Malcolm Mellor. Mechanical properties of polycrystalline ice. In Per Tryde, editor, *Physics and Mechanics of Ice*, pages 217–245, Berlin, Heidelberg, 1980. Springer Berlin Heidelberg. ISBN 978-3-642-81434-1.

[22] Malcolm Mellor and David M. Cole. Deformation and failure of ice under constant stress or constant strain-rate. *Cold Regions Science and Technology*, 5(3):201–219, 1982. ISSN 0165232X. doi: 10.1016/0165-232X(82)90015-5.

[23] Bernard Michel. *Ice mechanics*. Presses de l'université Laval, Québec, 1978. ISBN 0-7746-6876-8.

[24] P. O. Moslet. Field testing of uniaxial compression strength of columnar sea ice. *Cold Regions Science and Technology*, 2007(48):1–14, 2006. ISSN 0165232X. doi: 10.1016/j.coldregions.2006.08.025.

[25] Athanasios Papoulis and S. Unnikrishna Pillai. *Probability, random variables, and stochastic processes*. McGraw-Hill, Boston, 3rd ed. edition, 1991. ISBN 0070484775.

[26] Jürgen Plate. Auswertung von messwerten: Eine praxisorientierte einführung. 10.10.2016.

[27] Carl E. Renshaw, Narayana Golding, and Erland M. Schulson. Maps for brittle and brittle-like failure in ice. *Cold Regions Science and Technology*, 2014(97):1–6, 2014. ISSN 0165232X. doi: 10.1016/j.coldregions.2013.09.008.

[28] E.M Schulson. The brittle compressive fracture of ice. *Acta Metallurgica et Materialia*, 38(10):1963–1976, 1990. ISSN 09567151. doi: 10.1016/0956-7151(90)90308-4.

[29] Erland M. Schulson. The structure and mechanical behavior of ice. *JOM*, 51(2): 21–27, 1999. ISSN 1047-4838. doi: 10.1007/s11837-999-0206-4.

[30] Erland M. Schulson and Paul Duval. *Creep and fracture of ice*. Cambridge University Press, Cambridge, 2009. ISBN 9780511581397.

[31] J. Schwarz, R. Frederking, V. Gavrillo, I. G. Petrov, K.-I. Hirayama, M. Mellor, P. Tryde, and K. D. Vaudrey. Standardized testing methods for measuring mechanical properties of ice. *Cold Regions Science and Technology*, 1981(4):245–253, 1980. ISSN 0165232X.

[32] Seifaddini M., Aryanpour G., Farzaneh M. Structural properties and simple compression behavior of laboratory-made polycrystalline isotropic ice at high temperatures. (011501-10), 2018.

[33] John Snyder. *Tourism in the polar regions: The sustainability challenge*. UNEP, Nairobi, 2007. ISBN 928072813X.

[34] Lucie Strub-Klein and Denise Sudom. A comprehensive analysis of the morphology of first-year sea ice ridges. *Cold Regions Science and Technology*, 82:94–109, 2012. ISSN 0165232X. doi: 10.1016/j.coldregions.2012.05.014.

[35] Per Tryde, editor. *Physics and Mechanics of Ice*, Berlin, Heidelberg, 1980. Springer Berlin Heidelberg. ISBN 978-3-642-81434-1.

[36] L. M. Wachter, C. E. Renshaw, and E. M. Schulson. Transition in brittle failure mode in ice under low confinement. *Acta Materialia*, 57(2):345–355, 2009. ISSN 13596454. doi: 10.1016/j.actamat.2008.09.021.

[37] J. Xiao and I. J. Jordaan. Application of damage mechanics to ice failure in compression. *Cold Regions Science and Technology*, 24(3):305–322, 1996. ISSN 0165232X. doi: 10.1016/0165-232X(95)00014-3.

[38] Yue Q., Guo F., and Kärnä T. Dynamic ice forces of slender vertical structures due to ice crushing. *Cold Regions Science and Technology*, (56):77–83, 2009. ISSN 0165232X.